# TWO DIMENSIONAL RADIATION SENSOR DEVELOPMENT FOR USE IN SPACE BOUND RECONFIGURABLE COMPUTERS

by

Eric Christopher Gowens

A thesis submitted in partial fulfillment
of the requirements for the degree

of

Master of Science

in

Electrical Engineering

MONTANA STATE UNIVERSITY
Bozeman, Montana

May 2011

©COPYRIGHT

by

Eric Christopher Gowens

2011

All Rights Reserved

# APPROVAL

of a thesis submitted by

Eric Christopher Gowens

This thesis has been read by each member of the thesis committee and has been found to be satisfactory regarding content, English usage, format, citation, bibliographic style, and consistency and is ready for submission to The Graduate School.

Dr. Todd J. Kaiser

Approved for the Department of Electrical and Computer Engineering

Dr. Robert C. Maher

Approved for The Graduate School

Dr. Carl A. Fox

## STATEMENT OF PERMISSION TO USE

In presenting this thesis in partial fulfillment of the requirements for a master's degree at Montana State University, I agree that the Library shall make it available to borrowers under rules of the Library.

If I have indicated my intention to copyright this thesis by including a copyright notice page, copying is allowable only for scholarly purposes, consistent with "fair use" as prescribed in the U.S. Copyright Law. Requests for permission for extended quotation from or reproduction of this thesis in whole or in parts may be granted only by the copyright holder.

Eric Christopher Gowens

May 2011

## ACKNOWLEDGEMENTS

I am indebted to everyone who helped make this project possible. I would first like to thank my advisor and graduate committee chair, Dr. Todd Kaiser for all of his help and for giving me the opportunity to work on this project. I would also like to thank my other committee member, Dr. Brock LaMeres and Mr. Andy Olson for their assistance and valuable insights. Additionally I would like to thank Todd Buerkle for all the assistance he provided during this project. I also would like to thank my friends and family for the support they have offered throughout my work on this project. Finally, I would like to thank the National Aeronautics and Space Administration (NASA) for their financial support under the EPSCOR grant , which made this research possible

TABLE OF CONTENTS

1. INTRODUCTION TO SILICON SENSORS ........ 1

Introduction ........ 1
Basics of Semiconductor Physics ........ 1
P-N Junctions ........ 2
Junction Biasing ........ 4
Silicon Strip Sensors ........ 6
Statement of Problem ........ 7
Thesis Overview ........ 7

2. PREVIOUS SILICON STRIP SENSOR GENERATIONS ........ 8

Generation 1 Sensors ........ 8
Generation 1 Sensor Testing ........ 9
Generation 2 Sensors ........ 10
Generation 2 Sensor Testing ........ 11
The Drift Sensor ........ 15
Generation 3 Sensors ........ 15
Generation 3 Sensor Testing ........ 17
Generation 3 Sensor Testing Results ........ 21

3. GENERATION FOUR SENSOR DESIGN ........ 24

Introduction ........ 24
Sensor Design ........ 25
Die and Channel Size ........ 25
Bias Rings ........ 27
Doping Concentrations ........ 29
Mask Set ........ 30
Wafer Design ........ 31
Fabrication Sequence ........ 33

4. RESULTS OF GENERATION FOUR SENSORS ........ 34

Introduction ........ 34
Calculations and Modeling ........ 35
Calculations of Sensor Characteristics ........ 35
Built-in Voltage ........ 35
Full Depletion Bias ........ 35
Carrier Transient Times ........ 36
Charge and Current Generation from Radiation ........ 37
Modeling with COMSOL Multiphysics ........ 38

TABLE OF CONTENTS – CONTINUED

MATLAB Simulations of Internal Electric Field, Carrier Velocities, Transient Times, and Output Pulse Shape ....................40
Generation 4 Sensor Testing ....................43
Inter-Strip Resistance ....................43

Results of Infrared Laser Stimulation ....................44
Design Improvements ....................50
Two-Dimensional Multi-Channel Modeling ....................50
Non-Saturating Device Testing ....................51
Conclusions ....................52

5. PROJECT SUMMARY AND RECOMMENDATIONS FOR FUTURE RESEARCH ....................53

Summary ....................53
Recommendations for Future Research ....................53

REFERENCES CITED ....................55

APPENDICES ....................57

APPENDIX A: Generation 1 Sensor Response Plots ....................58
APPENDIX B: Generation 3 Sensor Measured Data ....................65
APPENDIX C: Mask Set Photographs ....................68
APPENDIX D: Fabrication Sequence ....................73
APPENDIX E: Calculations of Generation 4 Parameters ....................81
APPENDIX F: MATLAB Simulation Code ....................89
APPENDIX G: Generation 4 Sensor Data ....................93

# LIST OF FIGURES

Figure Page

1.1 P-N Junction at Equilibrium ....3

1.2 Strip Sensor Construction ....6

2.1 Generation 1 Sensor Structure ....8

2.2 Typical Response of Generation 1 Sensor ....9

2.3 Generation 1 Sensor LED Demonstration ....10

2.4 Front and Back Picture of Finished Generation 2 Sensor ....11

2.5 Response of Back Side of Generation 2 Sensor ....12

2.6 Absorption Depth vs. Wavelength in Silicon ....13

2.7 Output from Generation 2 Sensor Stimulated with Infrared Laser ....14

2.8 Micron Semiconductor Strip Sensor Structure ....16

2.9 Picture of the Front Side of Generation 3 Sensor ....16

2.10 Picture of the Back Side of Generation 3 Sensor ....17

2.11 Schematic of Biasing Scheme ....18

2.12 Picture of Power Supply Used for Biasing ....19

2.13 Generation 3 Infrared Laser Testing Apparatus ....19

2.14 Picture of Breadboard with Biasing Resistors ....20

2.15 Picture of Oscilloscope Used for Testing ....20

2.16 Output form Generation 3 Sensor ....21

2.17 Carrier Diffusion Distance vs. Doping Concentration ....23

3.1 Pictures of Amplification and Package Boards ....24

LIST OF FIGURES - CONTINUED

Figure Page

3.2 Pictures of a Finished Generation 4 Sensor, Front and Back ......................26

3.3 Pictures of a Packaged Generation 4 Sensor, Front and Back .....................27

3.4 Bias Ring Structure ........................................................................................28

3.5 Single Double-Sided Generation 4 Sensor Die from L-Edit .......................30

3.6 Die Placement on Wafer ..................................................................................31

3.7 Pictures of a Finished Wafer, Front and Back ............................................32

4.1 Micron Semiconductor Strip Sensor Structure ..........................................34

4.2 COMSOL Diffusion Simulation at 30ns.....................................................38

4.3 COMSOL Diffusion Simulation at 200ns...................................................39

4.4 COMSOL Diffusion Simulation at 470ns...................................................39

4.5 MATLAB Simulation of Device Characteristics at -10V Bias ...................40

4.6 MATLAB Simulation of Device Characteristics at -20V Bias ...................41

4.7 MATLAB Simulation of Device Characteristics at -30V Bias ...................42

4.8 Generation 4 Infrared Laser Testing Apparatus..........................................44

4.9 Picture of Infrared Laser Position on a Generation 4 Sensor.......................45

4.10 Plots of Generation 4 Performance with Infrared Laser
Aimed at Approximate Center of Sensor...................................................46

4.11 Plots of Generation 4 Performance with Infrared Laser
Aimed at Lower-Left Corner of Sensor .....................................................47

4.12 Plots of Generation 4 Performance with Infrared Laser
Aimed at Lower-Right Corner of Sensor...................................................47

LIST OF FIGURES - CONTINUED

Figure Page

4.13 Plots of Generation 4 Performance with Infrared Laser Aimed at Upper-Left Corner of Sensor ......................................................48

4.11 Plots of Generation 4 Performance with Infrared Laser Aimed at Upper-Right Corner of Sensor .....................................................48

4.12 Hole Diffusion Distance vs. Doping Concentration ...................................49

# ABSTRACT

Space bound computers are exposed to damaging radiation once they leave the safety of the Earth's atmosphere, which is a significant hindrance to the development of digital space systems. While most digital systems can be radiation hardened, the development time in making them less susceptible to radiation keeps the hardened systems behind the cutting edge. A better solution for this problem is to provide an early warning that a digital microchip may have been struck by radiation in the form of a spatially aware sensor. The focus of this thesis is the design, fabrication, and testing of a two-dimensional silicon-based radiation sensor capable of detecting the location of a potentially damaging radiation strike on a microchip. It is demonstrated that by using a strip sensor design, the spatial detection of incident radiation is possible. Simulations of performance are presented that predict the functionality of the strip sensor. The capabilities of a commercially available sensor are investigated. Additionally, a sensor is designed, fabricated, tested, and compared to the performance of the commercially available sensor. Recommendations for future research of the sensor design are discussed.

# CHAPTER ONE

# INTRODUCTION TO SILICON SENSORS

## Introduction

The use of silicon as the primary substrate in the semiconductor industry makes it a cheap, reliable, and effective platform for creating specialty sensors. Silicon-based sensors use crystalline silicon with regions of implanted impurities to create solid-state electrical devices. Devices that are manufactured in this way include photodiodes, avalanche photodiodes, and drift detectors. Each of these devices relies on the same semiconductor physical processes, which will be discussed in the following section.

## Basics of Semiconductor Physics

Semiconductor devices rely on two fundamental charge carriers: electrons and holes. Electrons (the elementary negative charge in an atom) are present in a silicon crystal in the form of covalent bonds that hold each atom in place in the crystalline lattice. With added impurities, such as phosphorus (which has one more electron than silicon), "free" or unbound electrons can be introduced into the silicon lattice. A region with a high concentration of implanted free electrons is known as an "N-type" region. The hole is the positive charge carrier within a semiconductor, but it is not a physical particle like an electron. A hole represents a broken covalent bond between neighboring atoms caused by an electron vacancy. In pure silicon holes are ideally not present, but adding impurities, such as Boron (which has one less electron than silicon), will

introduce holes in the lattice. An area with a high concentration of implanted holes is known as a “P-type” region. When holes and electrons are in close proximity, they will likely undergo a process known as recombination in which the electron fills the bond vacancy that is the hole, eliminating both free charge carriers.

P-N Junctions

When a P region and an N region are created in contact, a P-N Junction is formed. If left at equilibrium, the junction develops an area devoid of charge carriers called a depletion or space charge region. This is a result of there being a large concentration of holes (P region) next to a large concentration of free electrons (N region) and recombination occurring at the junction. The concentration of negative charge in the N region applies a “diffusion force” to the negative free electrons, pushing them to diffuse to the P side, and similarly holes are forced to diffuse to the N side by the concentration of positive charge in the P region. Once diffused, recombination occurs which leaves the area around the junction devoid of charge carriers, which is the depletion region.

The depletion region is devoid of free charge carriers, but a potential difference and corresponding electric field still exists across the junction. In the process of gaining or losing an electron to achieve a full valence band, the impurity atoms become positively or negatively charged (negative ions on the P side, and positive ions on the N side). This built in potential is a function of the doping concentrations of the P and N regions, and is given by Equation 2.1 [1], where T is temperature, k is Boltzmann’s constant, $N_A$ and $N_D$

are the acceptor and donor atom concentrations, and $n_i$ is the concentration for intrinsic silicon.

$$V_{bi} = \frac{kT}{q} \ln \left(\frac{N_A N_D}{{n_i}^2}\right) \qquad [1.1]$$

Equilibrium is reached when the opposing forces acting upon the charge carriers becomes equal. These opposing forces are the diffusion force which pushes carriers towards the junction and the built in field of the depletion region which pushes them away. A junction at equilibrium is illustrated in Figure 2.1.

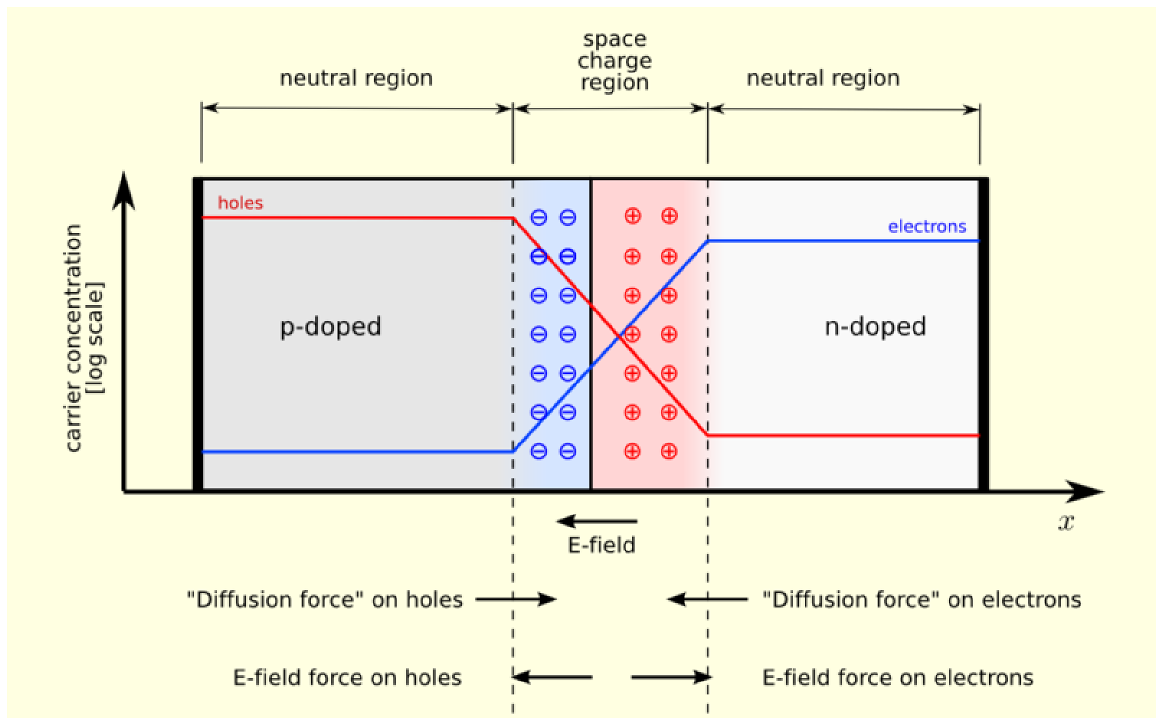


**Figure 1.1** An illustration of a P-N junction at equilibrium. [2]

Junction Biasing

By applying a biasing voltage across the junction, the behavior of the P-N junction can be changed. There are two modes of biasing a P-N junction: Forward biasing, where a positive voltage is connected to the P region (or a negative one to the N region), and reverse biasing, where a negative voltage is connected to the P region (or a positive one to the N region). Each biasing scheme directly affects the depletion region and the charge carriers in the junction.

Under a forward bias, the electric field from the potential difference between the P and N side is in the same direction as the diffusion force of their respective charge carriers. The biasing electric field pushes more charge carriers towards the junction, reducing the width of the depletion region. Once the depletion region is gone, the carriers can begin to move across the junction to recombine on the other side. At this point, the PN junction begins to conduct a current between its two sides.

When the junction is reversed biased, the electric field between the P and N sides is in the same direction as the field inside the depletion region. As the bias is increased, the depletion region widens by drawing holes away from the junction towards the edge of the P region, and drawing electrons away from the junction towards the edge of the N region. If a large enough bias is applied, the entirety of the PN junction becomes depleted. It is under this fully-depleted condition that most silicon sensors operate. The width of the depletion region for any given bias is directly dependant on the doping concentrations of the two regions, the built in voltage of the junction, and the applied bias voltage. The equation dictating the depletion width is shown in Equation 1.2 [1].

$$w_d = \sqrt{\frac{2\varepsilon}{q}\frac{N_A+N_D}{N_AN_D}\left(V_{bi}-V_{bias}\right)} \qquad [1.2]$$

Silicon Strip Sensors

A Silicon Sensor can be constructed in a variety of ways to detect incident radiation. The most basic method is a simple reversed biased P-N junction which will collect the charge generated by an ionizing radiation strike. While this method is effective in detecting the presence of radiation, it is incapable of providing any data beyond detection. A more attractive solution is presented in the strip sensor which uses multiple isolated P-N junctions on the same piece of silicon to provide the location of detected radiation.

By carefully designing a two-sided sensor, a radiation strike's location can be resolved in two dimensions. On one side (which will be called the front side for ease of reference), the silicon substrate will be doped with P-type material (usually boron) in parallel strips, or "channels." These channels of doped silicon will have a metal layer deposited on top to provide an electrical connection between the substrate and external electronics. The opposite side (backside) will be similarly constructed, but with its channels running perpendicular to the front side, and doped with an N-type material (usually phosphorus). The backside also has separate P-type regions implanted between the N-channels to electrically isolate them as the silicon substrate will short them together when reversed biased. The doped channels on the front and back of the silicon substrate

are effectively P-N junctions consisting of the channels and the bulk substrate. A more detailed diagram of the construction is shown in Figure 1.2.

Depletion regions form around the channel junctions, but to make the device more sensitive to ionization caused by radiation, a reverse biasing scheme must be used to fully deplete the substrate. When full depletion occurs, any EHPs generated by incident radiation will quickly be swept to the nearest channels by the internal electric field and collected. The two-dimensional position of the incident radiation is detected by monitoring which front and back channels collect the charge created. This principal is also illustrated in Figure 1.2.

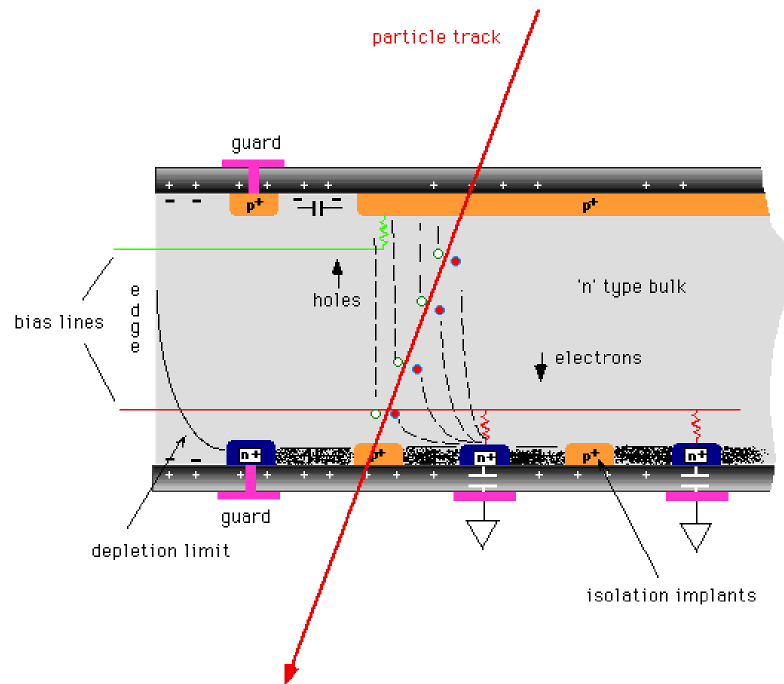


**Figure 1.2** A diagram of the strip sensors construction. Note: the topside of the sensor has a similar structure to the bottom, but it is perpendicular, which is why the side of only one channel is visible. Also, the bias lines are connected to the contacts on the outside and are not internal. [3]

## Statement of the Problem

The primary purpose of this research is to design, simulate, build and test a radiation detector capable of spatially resolving incident radiation in two dimensions, and compare it to a commercially available radiation sensor.

## Thesis Overview

To be able to accurately resolve the position of an ionizing radiation strike in two dimensions, a double-sided strip sensor design was chosen as the basic sensor design. A review of a previous sensor designs, and an investigation of a commercially available sensor are included in Chapter two. The design of the sensor this thesis focuses on is detailed in Chapter three. Chapter presents the simulation and experimental results of the newly designed sensor and a comparison between it and the commercial sensor. A project summary and recommendations for future work are included in Chapter five.

# CHAPTER TWO

# PREVIOUS SILICON STRIP SENSOR GENERATIONS

## Generation 1 Sensors

A former graduate student created a design for strip sensors that could be fabricated and used as a proof of concept in the NASA EPSCOR grant proposal. The first generation of sensors was fabricated as only a single-sided, one-dimensional sensor. The front side of the sensor is constructed in the same way as described in previous section, except there is an N+ "body contact" placed in one corner of the device, which was not used in this generation. The back side of the device consisted of just a blanket N+ layer over the entire back side with metal on top for electrical contact. As it was a proof of concept, the sensors were also fabricated on spare wafers that were available. The first and second generation sensors were fabricated on wafers with N-type substrates. An illustration of the sensors construction is shown in Figure 2.1.

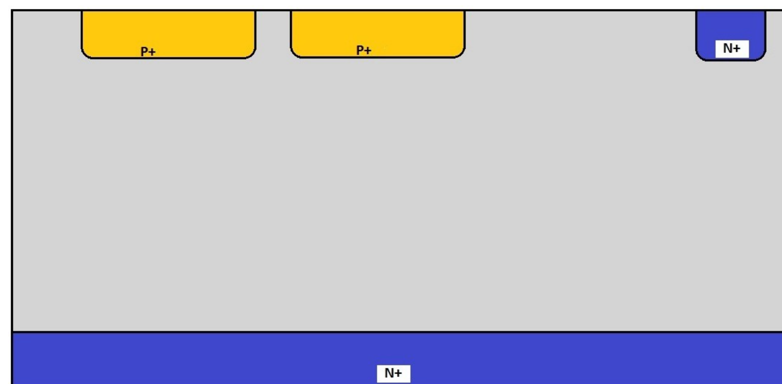


**Figure 2.1** An illustration of the structure of the first generation of sensors.

Generation 1 Sensor Testing

To test the performance of the single sided sensor, a red laser pointer was used to excite EHP generation on the surface of the sensor, while voltage and current measurements were taken at each channel. The voltage at each channel was measured in reference to the back side N+ plane, which was grounded. The results of this test for a typical die are available in Appendix A. A typical result is shown in Figure 2.2 where the laser is pointed at channel 5 on the sensor.

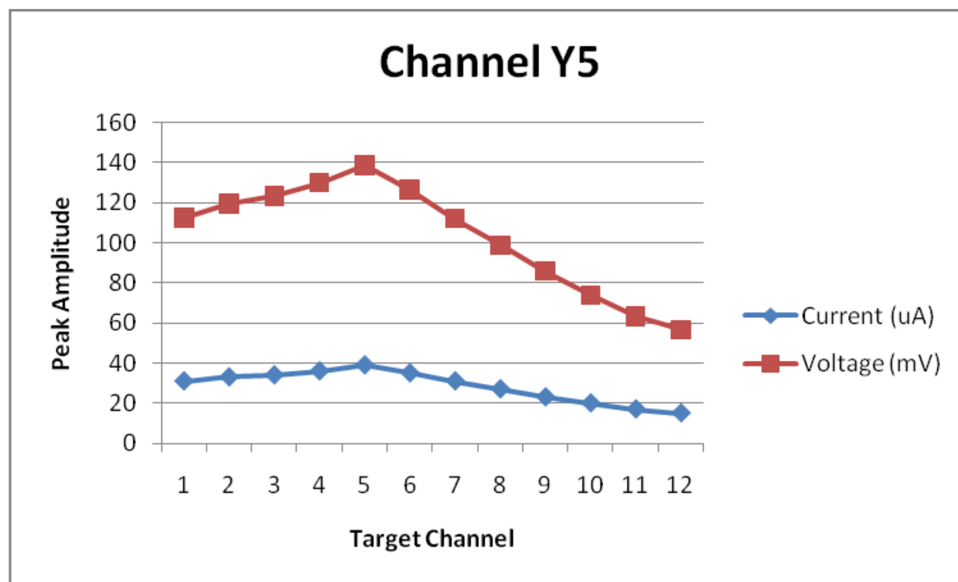


**Figure 2.2** A typical result from the generation 1 sensor. It can be seen that the laser is aimed at channel 5 by the fact that its response is above all other channels.

With the sensor output from the red laser test known, the single sided sensor was attached to a simple Op-Amp comparator circuit which lit up an LED. This set up was a simple way to physically represent when a channel was being hit by the laser. The set up and operation is shown in the photos of Figure 2.3.

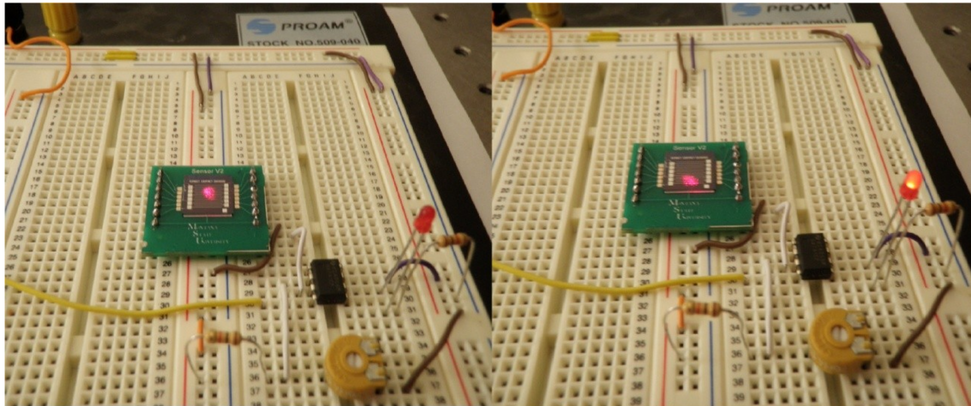


**Figure 2.3** Pictures illustrating the laser-LED test on the generation 1 sensor. The laser is not hitting the connected channel so the laser is off (left). When the laser hits the connected channel, the LED turns on (right).

The successful testing and application of the single-sided sensor led to the decision to use the same design and create a double-sided one with the hope of two-dimensional detection. The generation 2 sensor is the expansion of the single-sided design to a double-sided sensor.

## Generation 2 Sensors

Following the success of the single-sided, front side only sensors, it was decided to try creating double-sided sensors with the same structures on the front and back. The sensors were fabricated with two front sides, meaning that the channels on both the front and the back were made by implanting boron to make them P+ regions. The only difference was that the back side was turned 90 degrees with respect to the front side shown in Figure 2.4. As each side had the N+ body contact which was to be used as the reference in a differential measurement, it was assumed that the two sides would be able to operate independently.

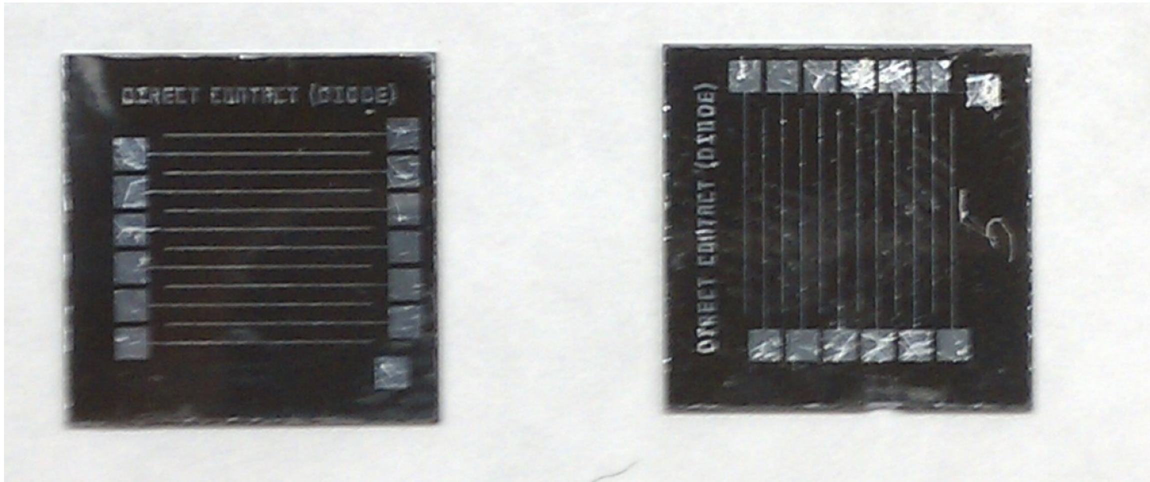


**Figure 2.4** Picture of the front and back of a generation 2 sensor. By convention, channel 1 is the top most channel, which is also furthest from the body contact.

<u>Generation 2 Sensor Testing</u>

To characterize the second generation of sensors, the same laser test used on the first generation was employed. The first measurements were taken by illuminating the channels directly with the red laser pointer and measuring the peak current output at every channel. Shown in Figure 2.5 is the best performing die found. It can be seen from the plot that the peak output decreases fairly linearly moving towards the body contact. This phenomenon was not understood at the time, but it was assumed that the addition of the back side structures was somehow interfering with the front side measurements. A red laser has a very small penetration depth in silicon, so all of the charge was being created on the surface of the die during testing. The decision was made to try using an infrared laser to stimulate the sensor, which would create charge throughout the substrate.

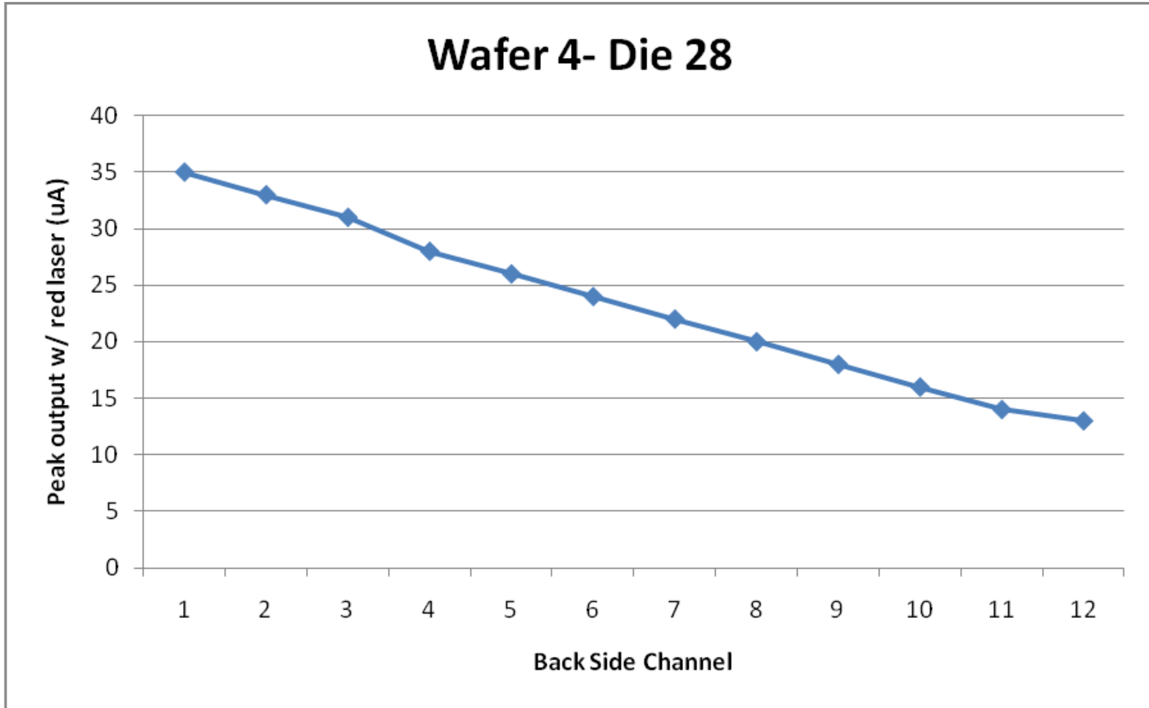


**Figure 2.5** Data taken from the back side of a second generation sensor. The peak current output drops off linearly approaching the body contact.

Silicon has the unique property of being highly transparent to infrared wavelengths, which makes an infrared laser an ideal solution for creating EHPs in the bulk substrate of a silicon sensor. Figure 2.6 shows the penetration depth of different wavelengths in silicon. The infrared laser used in testing the sensors has a wavelength of 808-1064nm, which gives it a penetration depth between 10 and 1000µm. The sensors were fabricated on wafers 525µm thick, making the infrared laser an attractive solution.

The peak output current was measured again sensors with the infrared laser, but with the illumination coming from the opposite side of the sensor from where the readings were taken. This was to ensure that charge was being created throughout the substrate, and not just on the surface. The results from the front and back of the same die

used in the red laser test are shown in Figure 2.7. The plot suggests that the illumination was not the problem in the measurements. Upon researching the geometry used in the sensors further, it was discovered that they were in fact drift sensors instead of strip sensors.

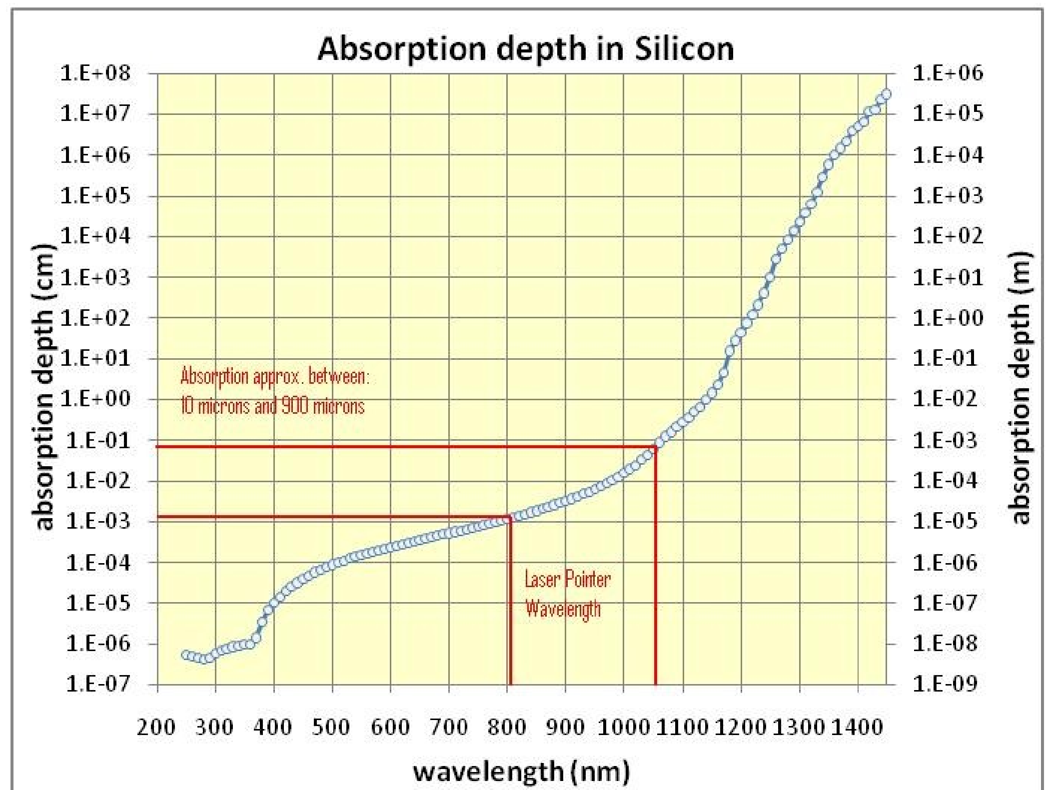


**Figure 2.6** Experimental data showing the absorption depth of different wavelengths in silicon. The wavelength and corresponding absorption depth of the infrared laser used in testing is shown in red. [4]

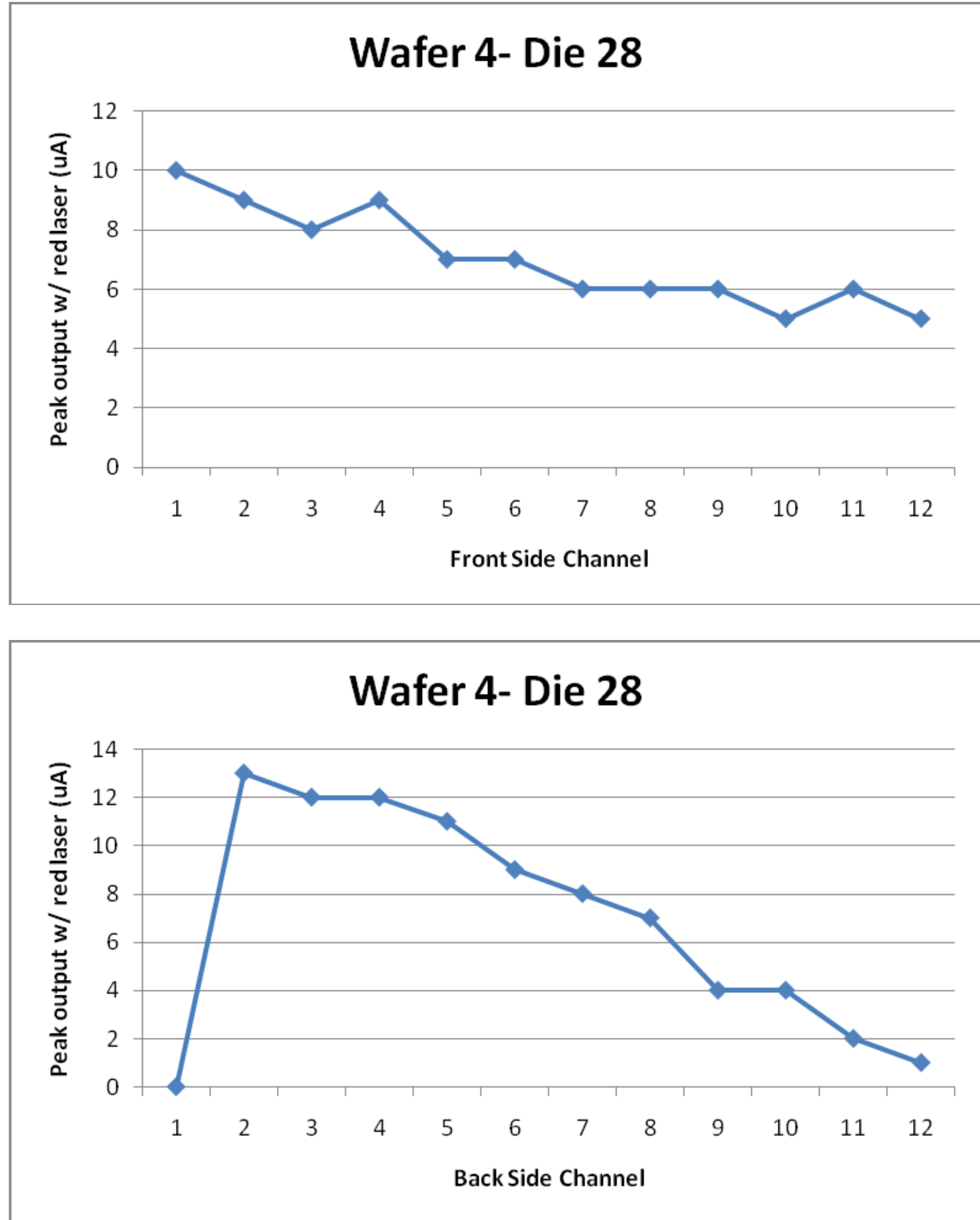


**Figure 2.7** Peak current output of the generation 2 sensor when stimulated with the infrared laser. The front channels were measured when the sensor was illuminated from the back (top plot), and the back side channels were measured when illuminated from the front (bottom plot).

## The Drift Sensor

The construction of the generation 2 sensor is actually known as a “drift sensor,” and not a strip sensor. Drift sensors function on the principal that electrons generated will be repelled by the P+ channels, and as such are propelled towards the N+ body contact. In an ideal drift sensor, the holes generated would be collected by a large P+ region on the back side of the sensor. With the generation 2 sensors, there is no large back side P+ region, so the holes are collected at each of the signal lines. It is for this reason that the results of the laser tests are less than ideal. As a result of the sensor outputs having this linear trend, use of the generation 2 sensors as strip sensors is extremely impractical. Without an even output across the channels, it becomes increasingly likely that a strike could produce enough charge that multiple channels could cross the threshold used by the sensor’s processing electronics and register a strike. This flaw in the design of the generation 2 sensors necessitates a redesign of the strip sensor.

## Generation 3 Sensor

To aid in understanding what kind of strip sensors were being used for industrial purposes, a commercially available sensor was purchased from Micron Semiconductor. The sensor has an ideal structure for a strip sensor, with sixteen channels constructed identically to the two shown in Figure 2.8. Additional pictures of the sensor’s actual appearance are shown in Figure 2.9 and 2.10.

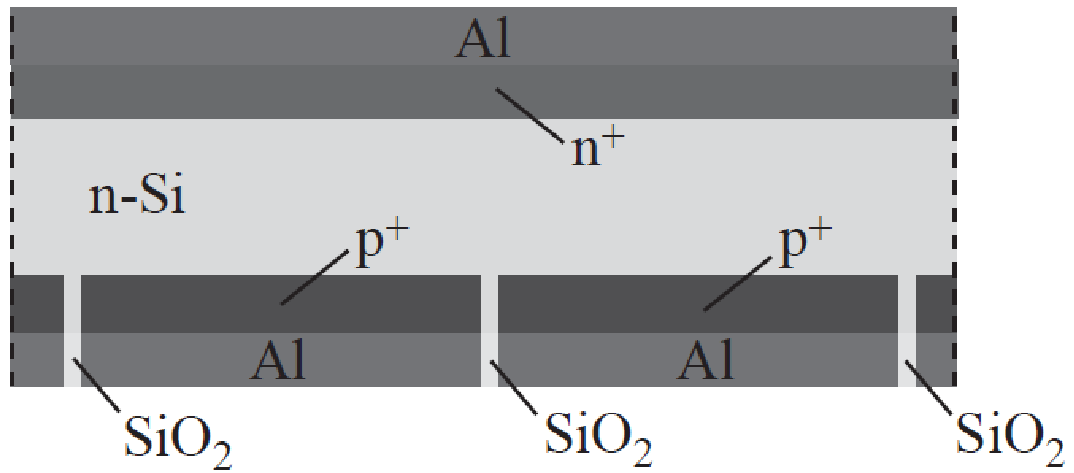


**Figure 2.8** Structure of the commercial Micron Semiconductor strip sensor. Note: The N-channels are perpendicular to the P-channels, so the picture only shows a side view of one channel. [5]

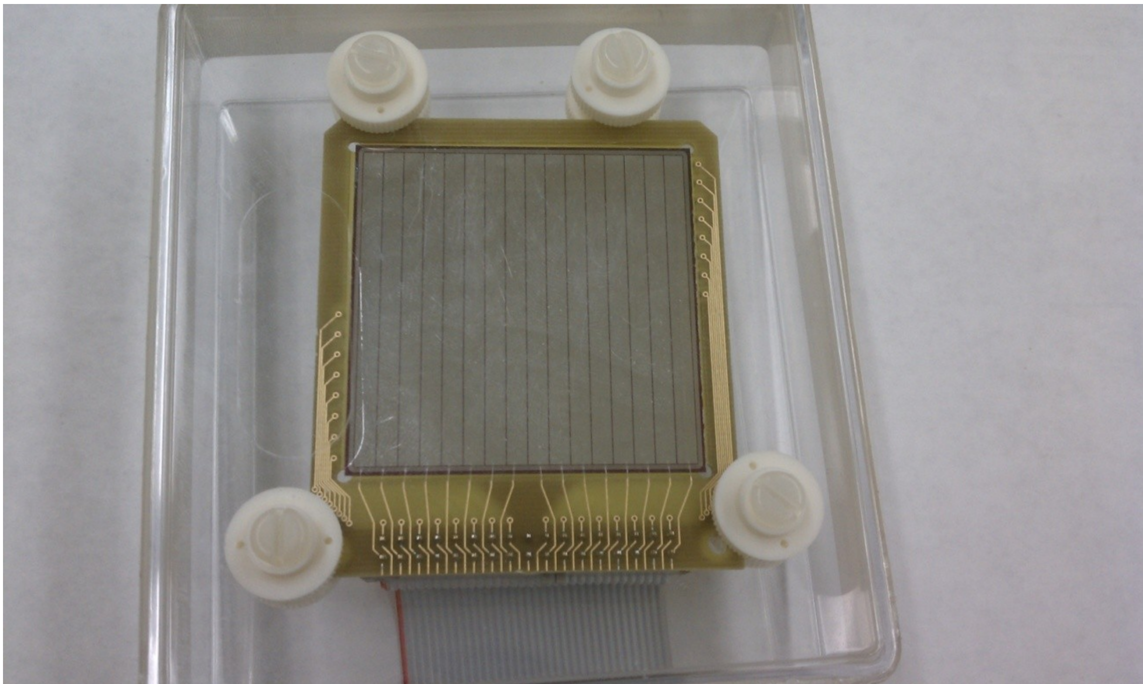

**Figure 2.9** Picture of the physical appearance of the front side of the Micron Semiconductor strip sensor.

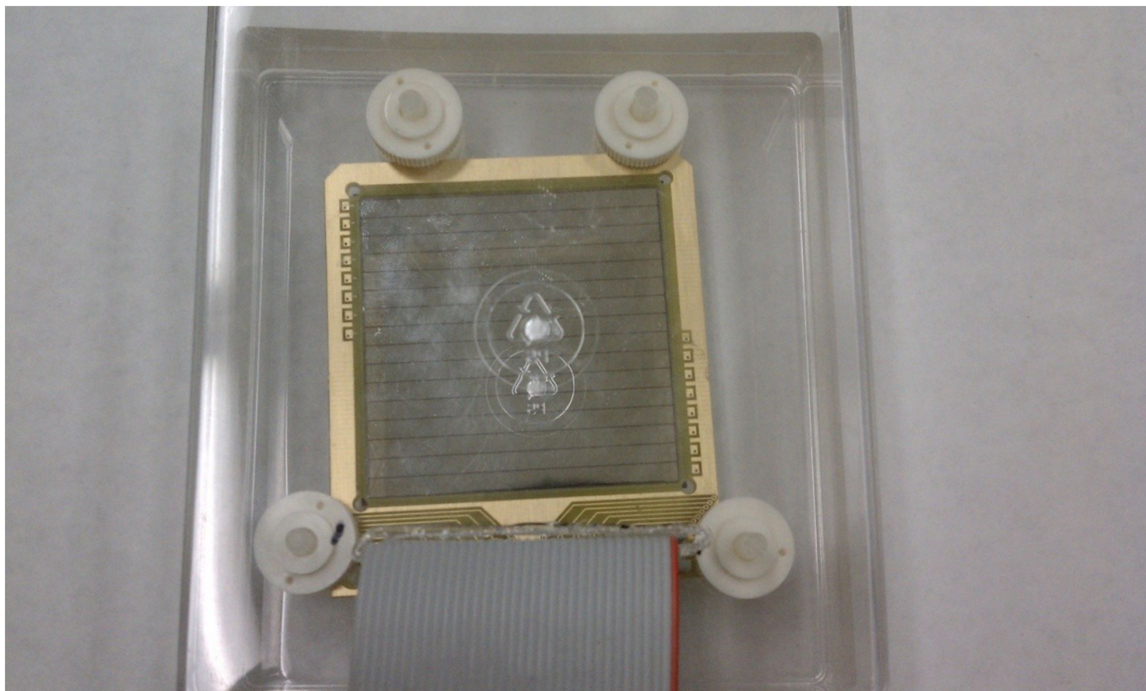

**Figure 2.10** Picture of the back side of the generation 3 sensor

To better understand the commercial sensor, it needed to be characterized in a way that was repeatable for future sensor production. The documentation included with the sensor outlined its ability to detect incident radiation, but this was not an experiment easy to reproduce reliably at MSU. Therefore, other metrics needed to be employed to discover what made a high quality sensor.

Generation 3 Sensor Testing

The first test implemented was a measurement of the inter-channel resistance on both the front and back sides of the sensor. As the sensor is sensitive to any ambient light, the measurements were taken with the sensor in complete darkness. The measured values

are available in Table B.1 in Appendix B. The inter-strip resistances are compared with the redesigned strip sensor's values in Chapter 4.

The second test was to use the infrared laser pointer to illuminate a spot on the sensor, and measure the output of all of the channels. For this test, the sensor's front side was connected to a negative bias voltage, and the back side was grounded to reverse bias the sensor. A schematic of the biasing scheme and test points is shown in Figure 2.11. The large resistors between the sensor and the biasing voltage/ground are in place to keep the generated charge from flowing directly to ground, or into the biasing power supply. When testing the generation 3 sensor, the laser pointer needed to be attenuated with the use of a neutral density filter so that it did not saturate the sensor. A chopper wheel was also used so that an AC-coupled measurement could be taken as the sensor's response is small compared to the applied bias voltages. Pictures of the set up are shown in Figures 2.12, 2.13, 2.14, and 2.15.

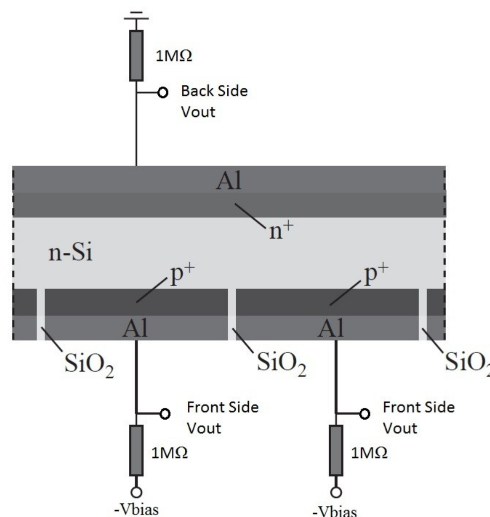


**Figure 2.11** Schematic detailing the biasing and testing scheme [5].

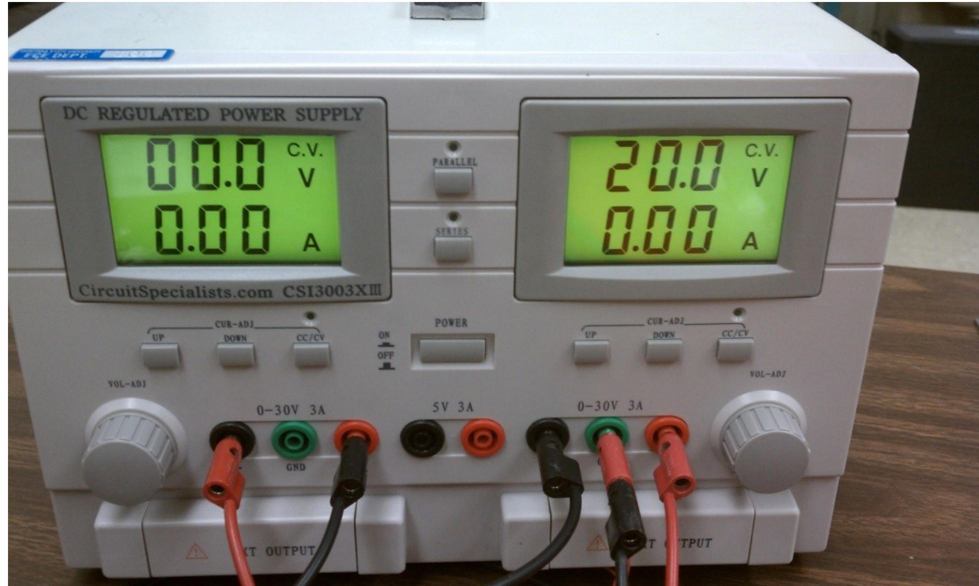


**Figure 2.12** The Circuit Specialists DC power supply used to reverse bias the sensor

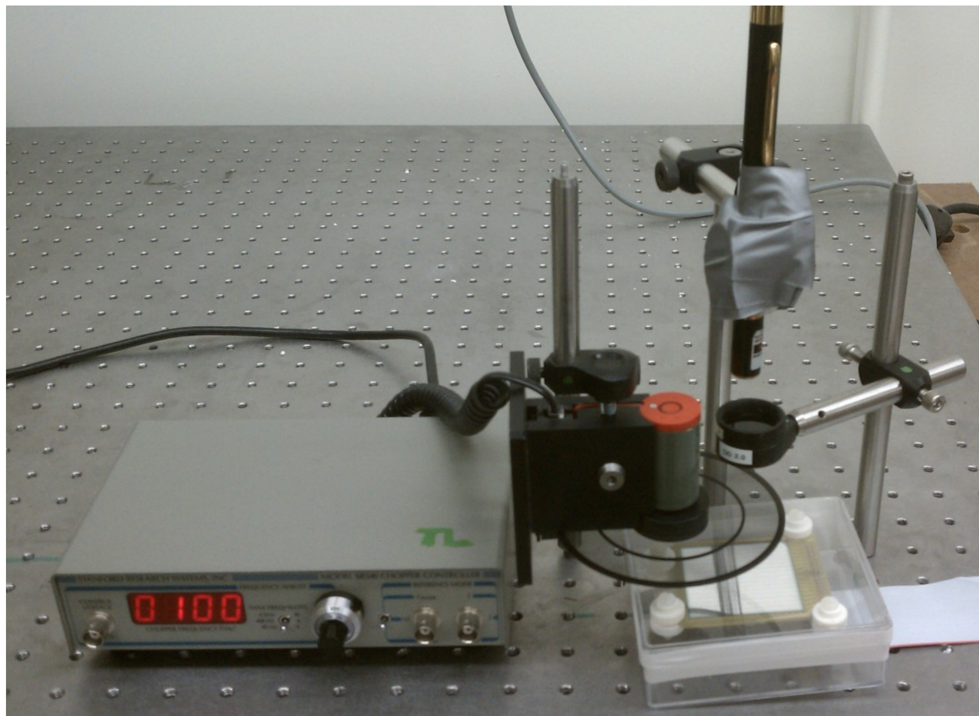


**Figure 2.13** Picture of the generation 3 sensor in the testing set up with the laser pointer, neutral density filter, and chopper wheel.

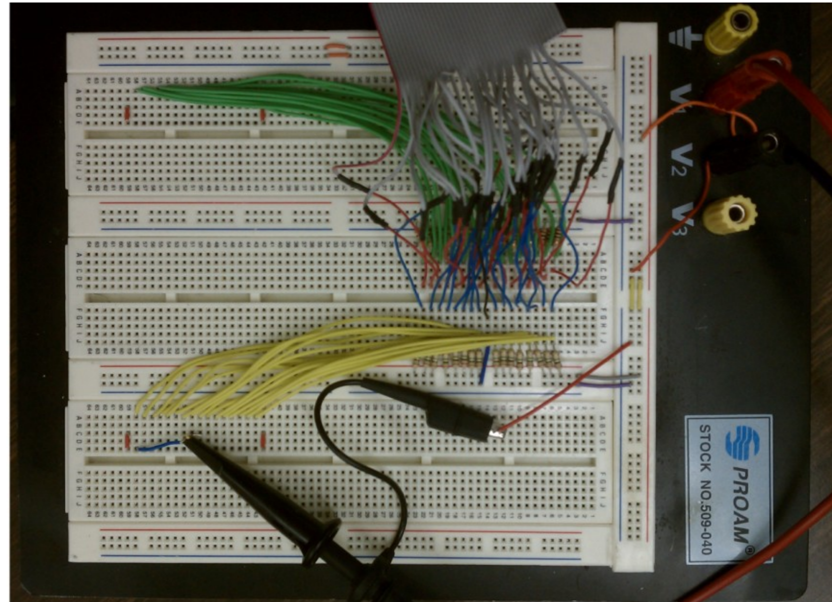


**Figure 2.14** Breadboard for testing set up. Note the rows of resistors between the sensor output and the ground and $V_{bias}$ lines

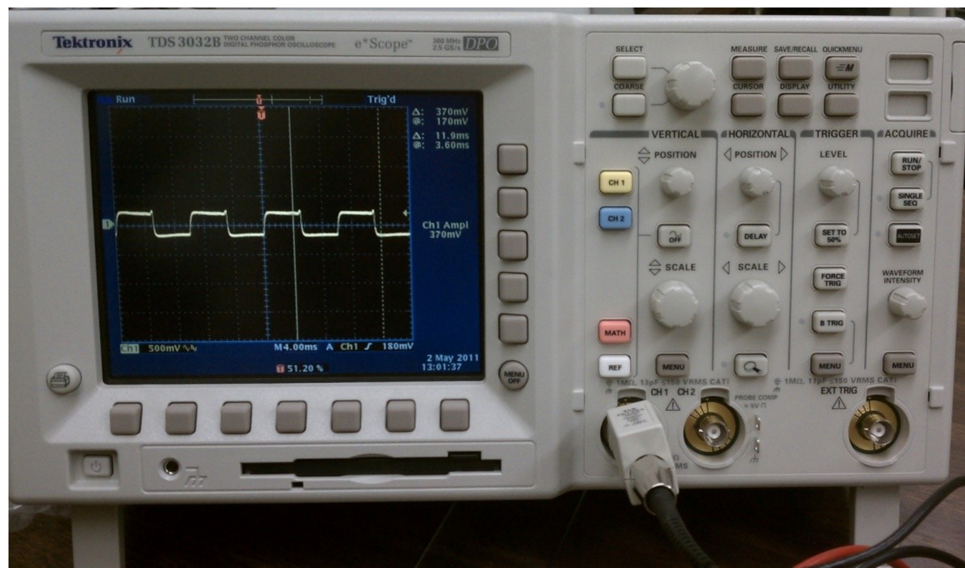


**Figure 2.15** A picture of the Tektronix oscilloscope used to test the sensor.

Generation 3 Sensor Testing Results

For the test, the laser was directed at the approximate center of the sensor, and each channel's output was tested individually. The measured voltages of each channel are available in Table B.2, in Appendix B. A graphical representation of the measured data is shown below in Figure 2.16. The data taken was normalized by subtracting the smallest measured value from every channel, to try and minimize the effect of lateral diffusion, then dividing by the largest measured value to give each channel a value between 0 and 1. The third column of plots in Figure 2.16 represents a comprehensive view of the two-dimensional location of the laser. These plots were created by adding every front side channel to every back side channel, then dividing each result by 2. This gives the three-dimensional plots shown, with magnitudes between 0 and1.

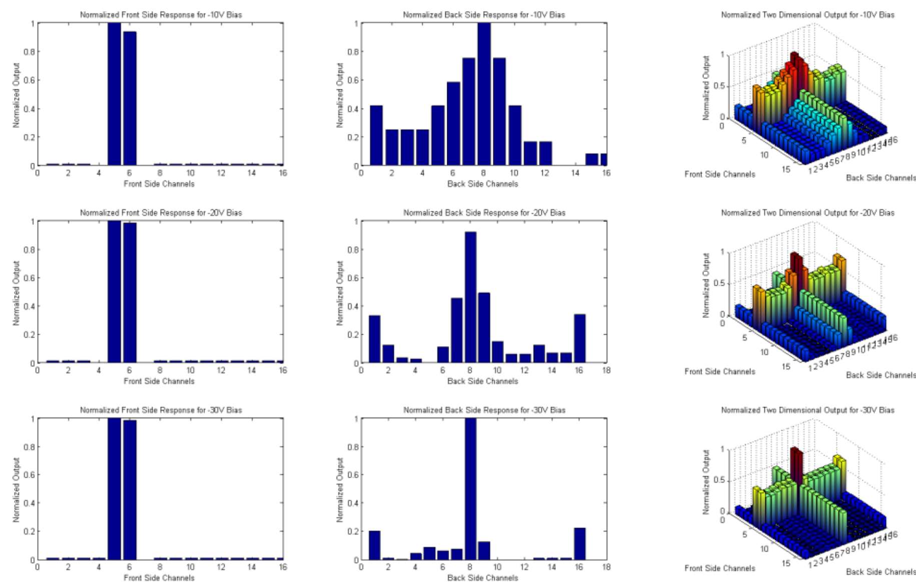


**Figure 2.16** Plots of the normalized front side (left column) back side (center column), and combined (right column) generation 3 data when biased with -10V (first row), -20V (middle row), and -30 V (bottom row).

It can be seen from the plots of Figure 2.16 that the performance of the generation 3 sensor is steadily improved by increasing the bias voltage applied. With increasing bias, the charge lost to neighboring channels not hit by the laser, especially on the backside, drops to nearly zero, which is the ideal case.

While the infrared laser test does provide a useful and easily repeatable method to test the sensors, it also causes an effect which wouldn't normally be seen from ionizing radiation. The sheer number of EHPs created in the substrate becomes a problem when using the laser. A radiation strike would usually cause a small line of charge to be created, on the order of 80 EHPs per micron of silicon [6], but the laser induces a substantially larger number, even when the chopper wheel is used to pulse it. The sudden creation of large amounts of EHPs causes them to laterally diffuse throughout the substrate. Once the charge diffuses, it is then collected by the channels. This becomes a problem when the laser hits channel 1, but the same output is seen on channel 16. The effect of lateral diffusion is even greater in low-doped silicon, like the substrate of the generation 3 sensor. In low-doped silicon, the charge carriers lifetimes and diffusion lengths are much larger, than in heavily doped silicon, as illustrated by Figure 2.17.

The large amount of lateral diffusion is the reason why the smallest measured value is subtracted from every channel of the generation 3 measurements before they are normalized to the largest value. This manipulation of the data produces plots that make the differences between neighboring channels much more obvious.

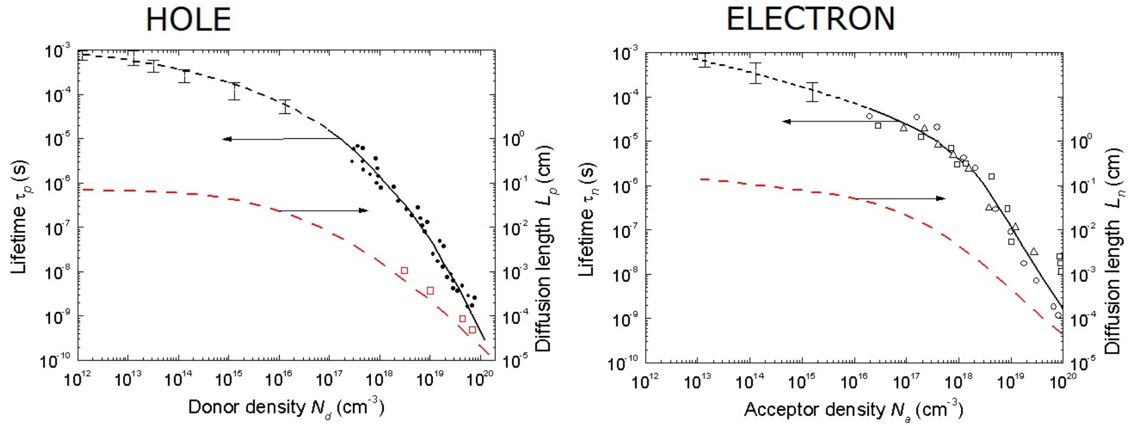


**Figure 2.17** Plots of carrier lifetimes and diffusion lengths vs. substrate doping [7].

While the commercial sensor has great performance, it is not well suited for our application. For one thing, the sensor is much too large, which decreases its spatial resolution. The active region of the sensor (the channels) is 50mm x 50mm, and the largest die size of the Xilinx FPGAs that will be used has a largest dimension of 16mm. This means the sensor is over three times as large as it needs to be to accommodate the Xilinx chip. Secondly, the cost of the commercial sensor is extremely restrictive if more than one were ever needed. Micron Semiconductor was kind enough to sell one on a 25% discount for $3,000. This price is much too high for the multiple sensors that will be needed for the reconfigurable computing project. The commercial sensor aided greatly in understanding the design and performance of a quality strip sensor, but it is not perfect for the project requirements. As a result of these drawbacks, a new sensor is designed that fits within the constraints of the project. The next chapter details the design of the fourth generation sensor.

# CHAPTER THREE

# GENERATION FOUR SENSOR DESIGN

## Introduction

The purpose of this research is to design and develop a silicon strip sensor capable of accurately resolving a strike by incident ionizing radiation in two dimensions. The sensor must be of sufficient size as to cover the largest Xilinx FPGA die, while providing fine enough resolution to detect if individual soft processors on the FPGA underneath it had been struck by the radiation. The other requirement of the sensor is that it must be similar in design to the generation 3 sensor, so that the two could use the same connector on an amplification board (Amp board) that will be used to shape, amplify, and digitize the signal generated by the sensors.  The Amp board is shown below in Figure 3.1 along with the package board that will hold and provide electrical contact to a completed sensor.

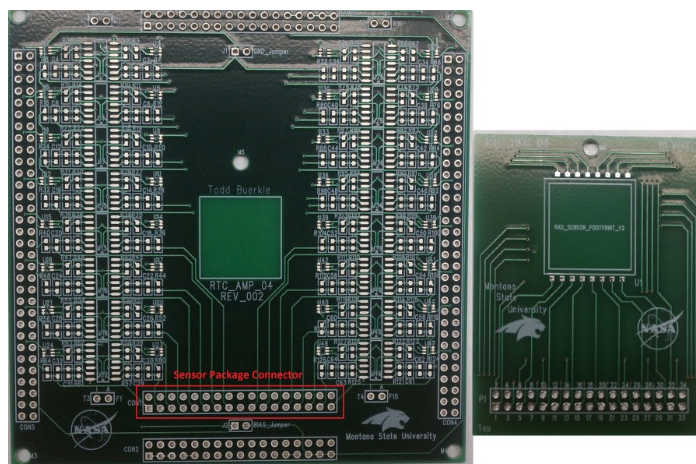


**Figure 3.1** Picture of the Amplification board that both the commercial sensor and the fourth generation sensor's package board will connect to (left), and the package board which will interface with the generation 4 sensor

## Sensor Design

Silicon was the obvious choice for a platform to build the strip sensor on, but intrinsic silicon was chosen above a doped variety for its natural lack of large concentrations of free charge carriers. With fewer free charge carriers in the substrate, the sensor is much easier to fully deplete (requires a lower bias voltage) than a substrate that has a high concentration of charge carriers. A silicon wafer that was double-side polished was also a necessity for the fabrication process as the sensor would need to be double sided. With these considerations in mind, 100mm diameter wafers were chosen from <www.el-cat.com> (item number D046) which are intrinsic with a resistivity of 20,000 to 30,000 Ω-cm, a thickness of 300±15μm, and double-side polished.

### Die and Channel Size

A die size of 20mm x 20mm for the sensor was decided upon to accommodate all Xilinx chip sizes that may be used in the reconfigurable computing project. This ensures that the sensor can detect incident radiation that may hit any point on the silicon die that makes up any Xilinx chip. The redesign of the strip sensor needed to be extremely similar to the commercial (third generation) sensor so that they could use the same connector on the amplification board shown in Figure 3.1. This requirement set the number of channels to 16 on the front side and 16 on the back side. Some area around the periphery of the die needed to be dedicated to identifying text and a bias ring structure, which will be discussed later, but the remaining area was used by the channels. A channel width of 1mm with 0.1mm spacing between channels was used as a conveniently round number

which would cover the vast majority of the die in active sensing area while leaving adequate room at the edges for the bias rings and text. To keep the die square and allow even spacing on all sides, the necessary channel length was 18.77mm. The 0.1mm spacing between channels was also chosen to provide electrical isolation between the channels so that charge diffusion could be kept at a minimum. The front and the back sides of the sensor utilize this same channel size and spacing to keep the sensing area even on the front and back even though the backside does not have the bias ring structure. Pictures of the front and back of a finished sensor and of a packaged sensor are presented in Figure 3.2 and 3.3 respectively

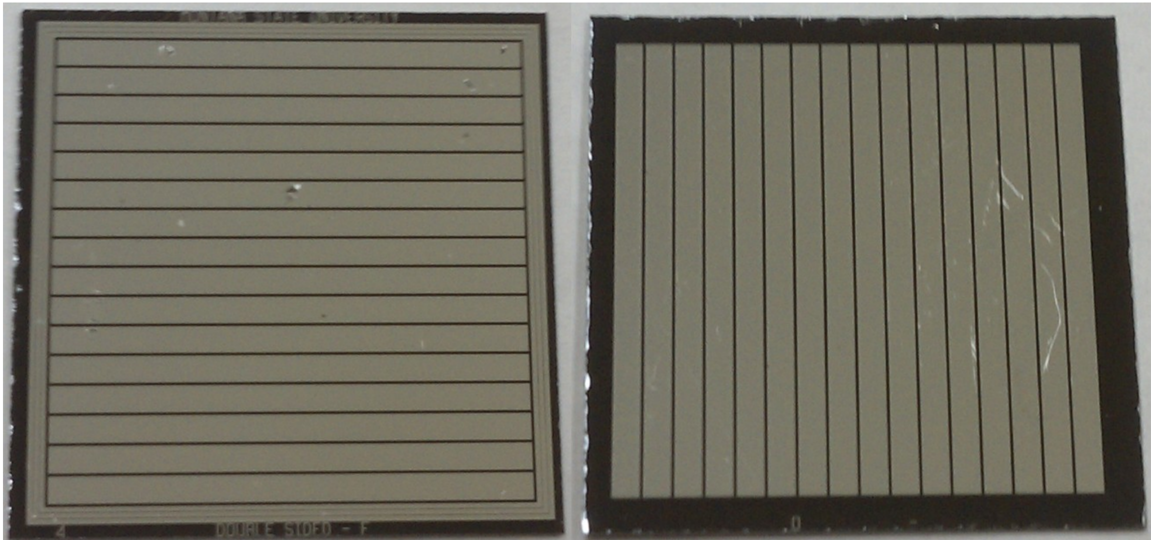


**Figure 3.2** A picture of the front and back of a finished generation 4 sensor

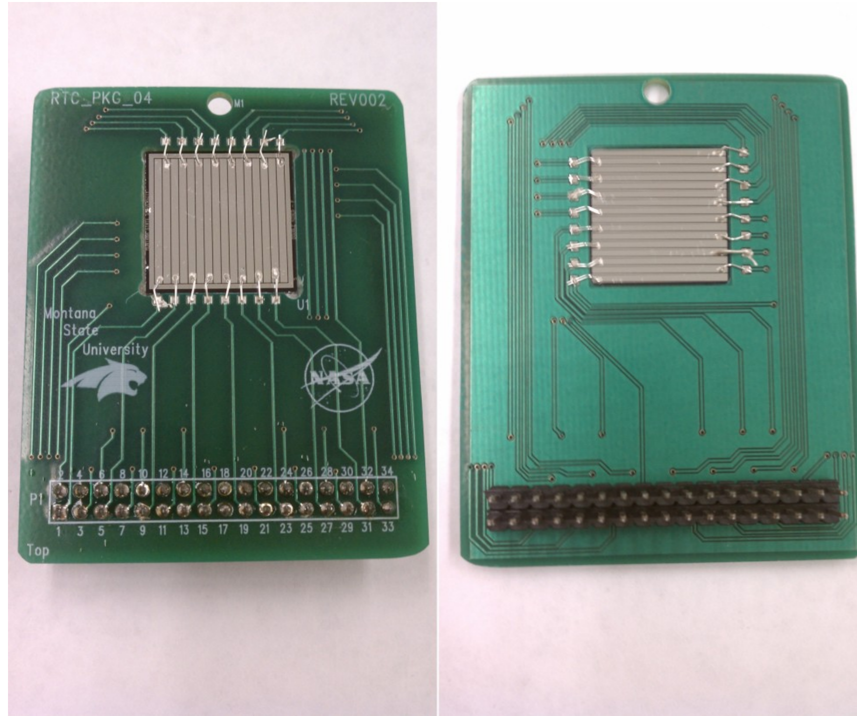


**Figure 3.3** Pictures of the front (left) and back (right) of a packaged completed generation 4 sensor

<u>Bias Rings</u>

The bias rings are an attempt to stabilize the long term performance of the sensors over a variety of external conditions. The need for the guard rings arises out of observations of fully depleted silicon sensors suffering from charge build up on oxide surfaces which can culminate in expanding the depletion region to the cut edge of the silicon die. If the region reaches the edge, the damaged crystal lattice will enable electron-hole pair generation resulting in the reverse current increasing by orders of magnitude [8]. In essence, the bias rings are there to guard against high potentials and electric fields at the cut boundary of the silicon die. It should be noted that the generation 3 sensor also has bias rings to counteract this effect.

The structure of the bias rings consists of three concentric rings encircling the entire sensor area. The rings act as a series of MOSFETs with the gates and sources connected to gradually decrease the bias voltage towards the edge of the sensor. If the voltage difference between two neighboring rings is greater than the threshold in the reverse direction, the neighboring rings will conduct. This keeps the voltage low at the edge of the die. These bias rings were included in the design to keep the generation 4 sensor as close to the generation 3 sensor as possible. They were also included as a future experiment for whenever the long-term performance of the sensor is investigated. An illustration of the bias ring's structure is shown in Figure 3.4.

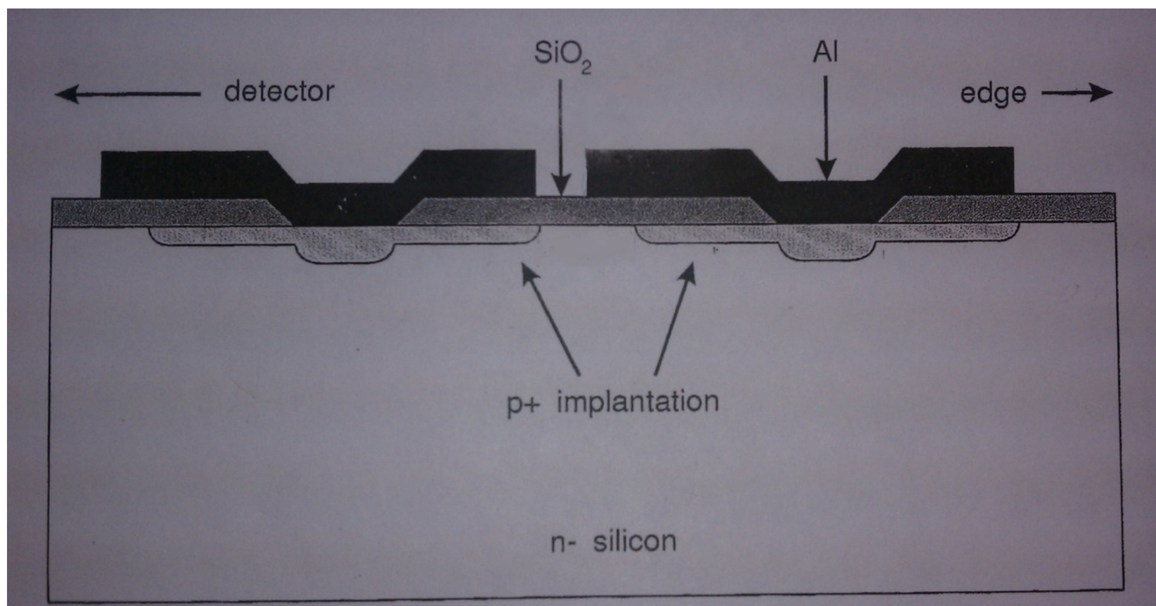


**Figure 3.4** An illustration of the structure of the bias rings.

Doping Concentrations

As previously stated, the front side consists of 16, evenly spaced boron doped (P+), channels with a surrounding ring structure, also doped with boron at the same time as the channels. The doping concentrations of the channels had no constraints except that it needed to have a much higher concentration of charge carriers than the intrinsic substrate to provide collection for the holes generated by ionizing radiation. It was calculated that the intrinsic wafers were not perfect, but had a background electron concentration of $2.15x10^{11}$ $cm^{-3}$ [9]. A perfectly intrinsic substrate would have a carrier concentration of roughly $1.0x10^{10}$, which means the substrate used is slightly N-type. With this in mind, it was decided that a concentration on the order of $1.2x10^{20}cm^{-3}$ would be a sufficient concentration for the front side channels and bias rigs.

The back side of the sensor is similarly constructed to the front side in the fact that is also has 16, evenly spaced doped channels. However, the backside channels are doped with phosphorus (N+) to provide collection for the electrons generated by ionizing radiation. Again with the substrate's slight doping in mind, a phosphorus concentration of $2.2x10^{20}cm^{-3}$ is sufficiently larger than the background concentration. Since both the channels and the substrate are N-type materials, there was concern that conduction would occur between neighboring cannels by the substrate effectively shorting them together. To negate this effect, the channels were electrically isolated by implanting strips of boron between, above and below the channels. To ensure that the channels were sufficiently isolated, a concentration of $1.2x10^{20}cm^{-3}$ of boron atoms was diffused in as a barrier, which is relatively high when compared to the concentration of the substrate.

## Mask Set

With the general design of the sensor finished, a mask set was designed and fabricated for use in manufacturing the sensors. A total of seven masks were needed to pattern the front side channels, back side channels, backside barriers, front side contacts, back side contacts, the front side metal, and the back side metal. Each mask was designed as a separate layer in L-Edit. A picture of a single die showing all the layers in L-Edit is shown in Figure 35. The masks were fabricated by patterning aluminum on 5in x 5in glass plates by the University of Minnesota's Nanofabrication Center. Pictures of Each mask are shown in Appendix C.

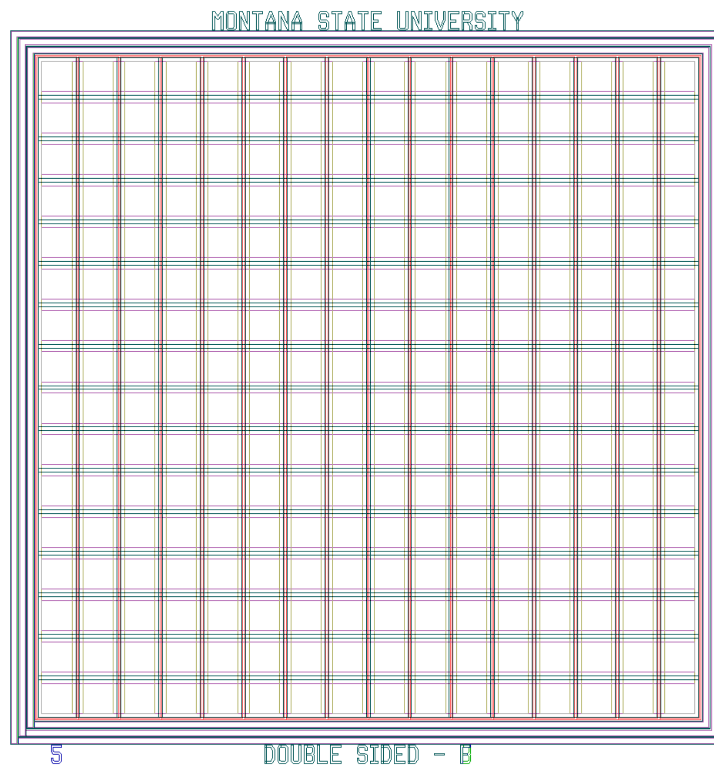


**Figure 3.5** A picture of a single double-sided die with all of its layers visible in L-Edit.

Wafer Design

As previously noted, the sensors are fabricated on 100mm diameter silicon wafers. This allows enough room to comfortably fit 9 different sensors. Five different sensor variants were constructed on each wafer to allow testing of all structures individually to help diagnose problems. Each wafer included one front side only sensor, which had a blanket N+ doping on the back side instead of channels, two back side only sensors, both of which had a blanket P+ doping on the whole front side (one of the back side only sensors was also created without the P+ barrier diffusions between the channels), one double sided sensor that was created without the P+ barrier diffusions between the back side channels, and five ideal double sided sensors. The layout of the sensors is shown in Figure 3.6, and pictures of the front and back of a completed wafer are shown in Figure 3.7.

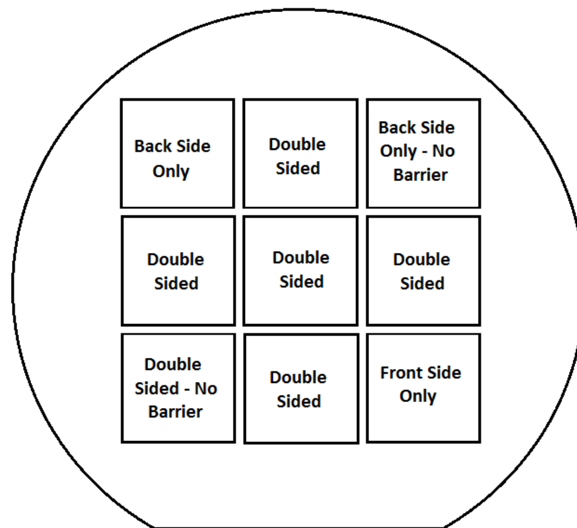


**Figure 3.6** Illustration of the placements of sensor variants on a wafer

The deliberate placement of the full double sided sensors was to compensate for any edge effects that may occur during the various diffusions. In previous experiences with the diffusion furnaces, problems with doping close to the edge of wafers have been observed. By placing the most important sensors in the five spots furthest from the wafers edge, the likelihood a diffusion problem negatively affecting them is minimized.

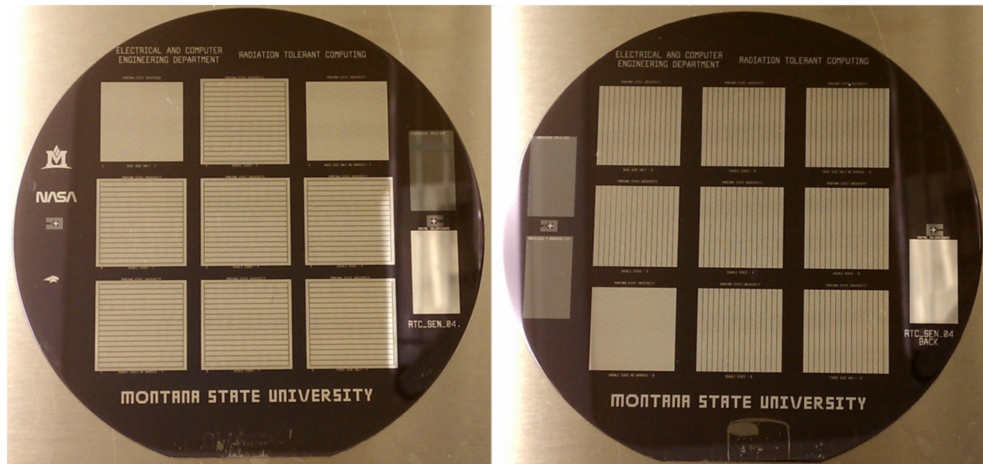


**Figure 3.7** Picture of the front (left) and back (right) of a completed wafer of sensors.

The other large structures that can be seen on the wafers in Figure 3.4 are windows to areas of the substrate that have undergone the different diffusions. The purpose of these windows is to provide test points for determining the quality each diffusion. The upper window on the front side is a P+ doped region with the same characteristics of the front side channels. The bottom rectangle is simply a sheet of aluminum deposited at the same time as the channel's metal contacts. The upper left window on the backside is for the N+ channel diffusion, and the lower left window is for

the P+ barrier diffusion. The window to the right on the back side is also a sheet of aluminum deposited with the backside channel's metal contacts.

## Fabrication Sequence

This section gives a brief overview of the most important parameters of the fabrication sequence, the diffusions. A full description of the fabrication is given in Appendix D.

Front Side P+ Channels:

| | |
|---|---|
| Diffusion Source: | Boron – 1 source for every 2 wafers |
| Temperature: | 950° C (1223K) |
| Time: | 60 minutes |
| Gas Flow: | Nitrogen at a flow of $7cm^3$/min |

Back side N+ Channels:

| | |
|---|---|
| Diffusion Source: | Phosphorus – 1 source for every 2 wafers |
| Temperature: | 900° C (1173K) |
| Time: | 30 minutes |
| Gas Flow: | Nitrogen at a flow of $7cm^3$/min |

Back side P+ Channels:

| | |
|---|---|
| Diffusion Source: | Boron – 1 sourComputerce for every 2 wafers |
| Temperature: | 950° C (1223K) |
| Time: | 30 minutes |
| Gas Flow: | Nitrogen at a flow of $7cm^3$/min |

# CHAPTER FOUR

# RESULTS OF GENERATION FOUR SENSORS

## Introduction

The double sided strip sensor design detailed in Chapter Three is based on the general sensor design by Micron Semiconductor, which is repeated in Figure 4.1. A characterization of the fourth generation sensors is a necessity to compare their performance to that of the commercial sensor detailed in Chapter Two. This chapter first presents simulated results, followed by measurements of the fourth generation sensor. Finally, the performances of the fourth generation sensor and the commercial sensor are compared and discussed.

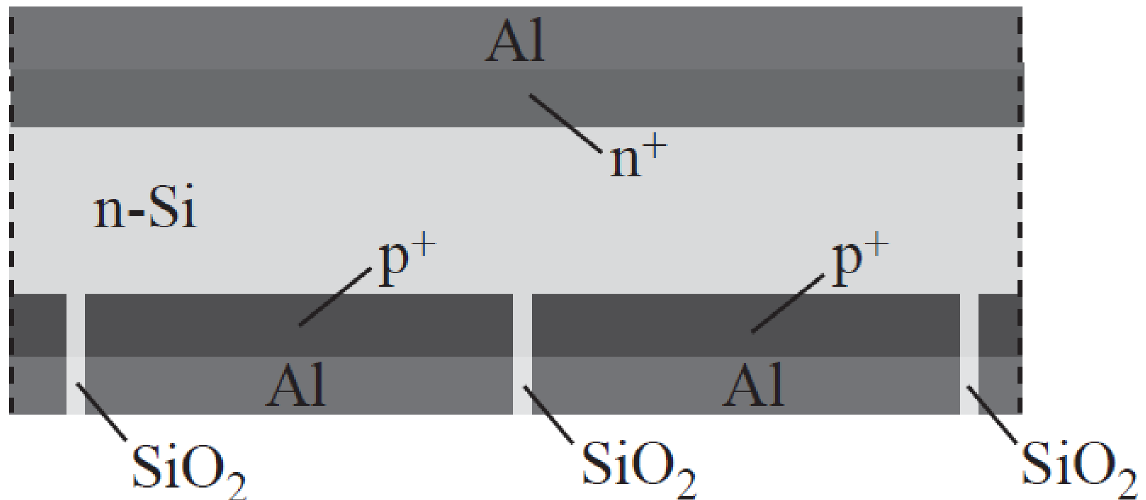


**Figure 4.1** Structure of the commercial Micron Semiconductor strip sensor.

Note: The N-channels are perpendicular to the P-channels, so the picture only shows a side view of one channel. [5]

# Calculations and Modeling

This section will present calculations and modeling of the fourth generation sensor based upon measurements of its characteristics taken during fabrication.

## Calculations of Sensor Characteristics

A first order estimate of the basic semiconductor properties of the sensors is important for developing a comprehensive understanding of their operation. To develop this approximation, the expected built in voltage, full depletion bias voltage, maximum carrier transient times, and radiation-generated charge and current are calculated. Further calculations and a more detailed approach to the proceeding calculations are included in Appendix E.

Built in Voltage: The built in voltage at the implanted junctions is calculated using Equation 1.1 [1] (repeated here as Equation 4.1 for convenience).

$$V_{bi} = \frac{kT}{q} \ln \left(\frac{N_A N_D}{{n_i}^2}\right) \qquad [4.1]$$

From the measured values of the concentrations $N_A$ and $N_D$, the built in voltages for the front side P+ channel and the back side N+ channel junctions are 0.63V and 0.62V respectively.

Full Depletion Bias Voltage: The biasing voltage required for full depletion is calculated by solving Equation 1.2 for $V_{bias}$ and applying the calculated built in voltage, which yields Equation 4.2.

$$V_{bias} = V_{bi} - \frac{w^2 q N_A N_D}{2\varepsilon_r \varepsilon_o (N_A + N_D)} \qquad [4.2]$$

The sensor biasing occurs by applying a negative voltage to the P+ channels while grounding the N+ channels. This implies that the expansion of the depletion region comes exclusively from the biasing applied to the P+ channels. The N+ channels have an inherent depletion region, but it is much smaller than the region supplied by the P+ biasing. As a first order approximation, the effect of the N+ depletion region is ignored, and the full depletion biasing voltage is calculated using just the P+ junction effects alone. By using this approximation, the sensor becomes fully depleted when biased when $V_{bias}$ = -14.07V.

Carrier Transient Times: To find the maximum carrier transient time, which is the time needed for a charge carrier to cross the total thickness of the device, the electric field must be known. The average electric field provides a useful approximation from which the transient times are derived. The average electric field is approximated by dividing the voltage difference between the two sides of the sensor ($V_{bias}$) by the sensor's thickness in centimeters (0.03cm), as shown in Equation 4.3. This yields an average electric field of $E_{ave}$ = 496.0 V/cm.

$$E_{ave} = \frac{V_{bias}}{thickness} \qquad [4.3]$$

With a known electric field across the sensor, the carrier velocities can be calculated by multiplying the carrier mobility by the average electric field as shown below.

$$v_{carrier} = \mu_{carrier} * E_{ave} \qquad [4.4]$$

Equation 4.4 gives an electron and velocity of $v_e$ = 6.631E+05cm/s and a hole velocity of $v_h$ = 2.206E+05cm/s. Finally, the maximum carrier transient times are calculated by dividing the maximum distance traveled of 0.03cm by the velocities, as given by Equation 4.5:

$$t_{carrier} = \frac{v_{carrier}}{thickness} \quad [4.5]$$

This yields a maximum electron transient time of $t_e$ = 45.24ns and a hole transient time of $t_h$ = 135.97ns

Charge and Current Generation from Radiation: It is known that, on average, ionizing radiation generates 80 EHP/µm in silicon [6]. By multiplying this value by the thickness of the sensor, the average amount of charge can be approximated shown in Equation 4.6:

$$Q = 80 * thickness * q \quad [4.6]$$

This yields an average of 24000 EHP, and a charge of $Q$ = 3.84E-15C generated in the sensor. By expanding Equation 4.6 to include the carrier transient times, an approximation of the current generated on both the front and back side channels is created, as shown by Equation 4.7:

$$I = \frac{80 * thickness * q}{t_{carrier}} \quad [4.7]$$

By applying the previously calculated carrier transient times, the electron current $I_e$ = 8.49E-8A and the hole current $I_h$ = 2.82E-8A emerge.

The values calculated above give a reasonable first order approximation of an average sensor's performance, based upon measurements of physical parameters of wafer Rad4-6 during its fabrication

Modeling with COMSOL Multiphysics

A simple COMSOL model was created to show the differences in the electron and hole mobilities. The first order model consists of a line of positive and negative charge carriers being created in bulk silicon with an applied electric field to mimic a biased sensor. The still frames shown in Figure 4.2, 4.3, and 4.4 explain what happens to charge distributions created inside the sensor over time. It can be clearly seen that the holes (red and yellow) diffuse at a much slower rate than the electrons (blue). It should also be noted that the holes tend to diffuse much farther laterally before being absorbed at the edge of the sensor.

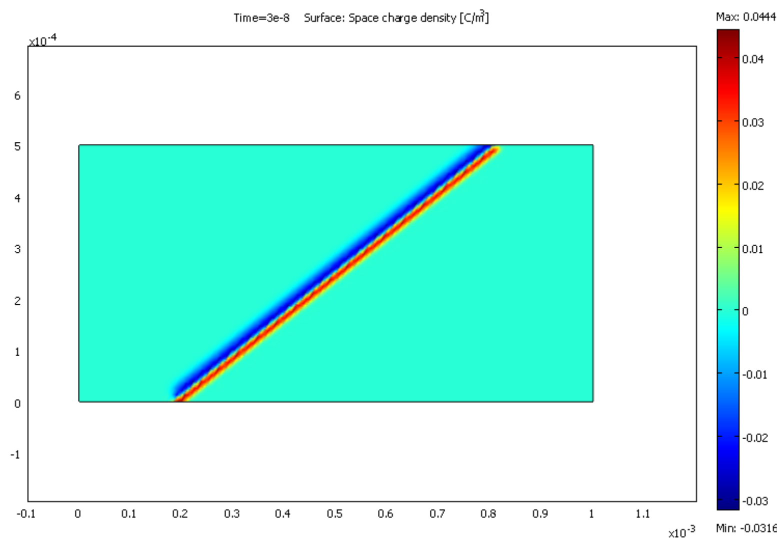


**Figure 4.2** The beginning of the simulation. The line of charge has just been created. Electrons are shown in blue, and holes are shown in red and yellow.

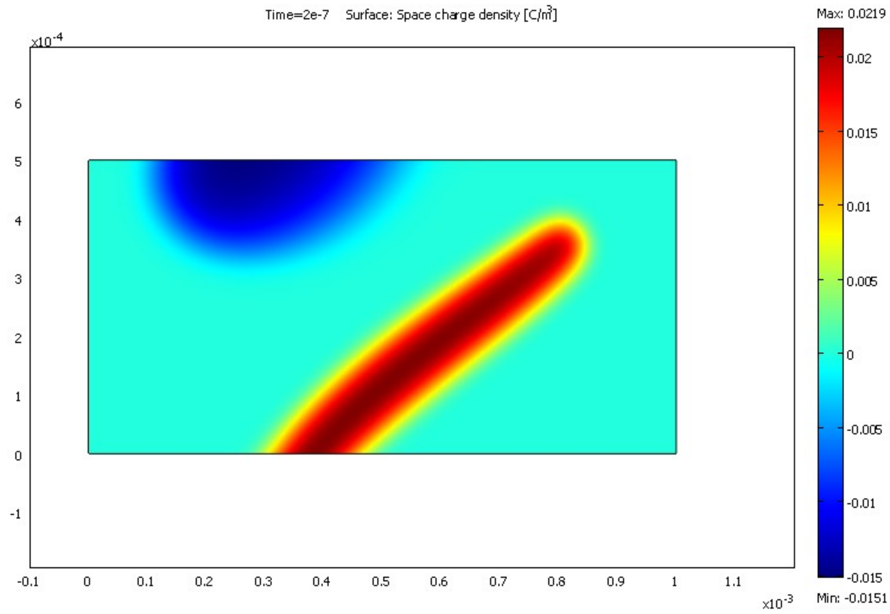


**Figure 4.3** The charge distributions have changed position and shape after 200ns. Electrons are shown in blue, and holes are in red and yellow.

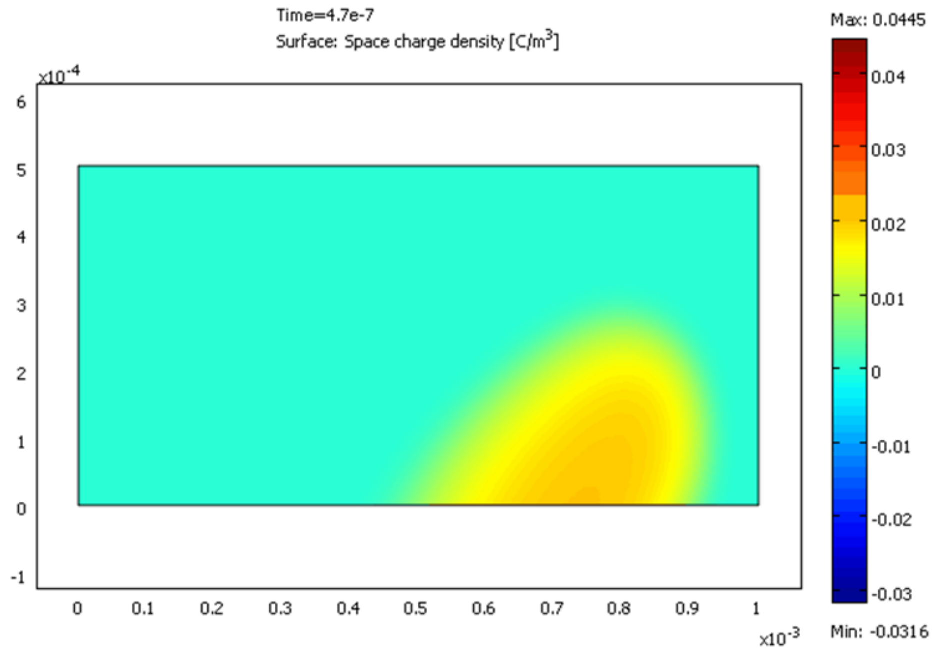


**Figure 4.4** Charge distributions after 470ns. Only holes (yellow) remain.

MATLAB Simulations of Internal Electric Field,
Carrier Velocities, Transient Times, and Output Pulse Shape

By using MATLAB to calculate the electric field internal to the sensor, a second order approximation can be made of the electric field distribution, carrier velocities, transient times, and the current output of the sensor at different bias voltages. The plots shown in Figures 4.5, 4.6, and 4.7 show the different parameters mentioned above, when the sensor is biased at -10V, -20V, and -30V respectively. The origin of the position parameter is placed at the surface of the front side of the wafer. The code for these simulations is available in Appendix F.

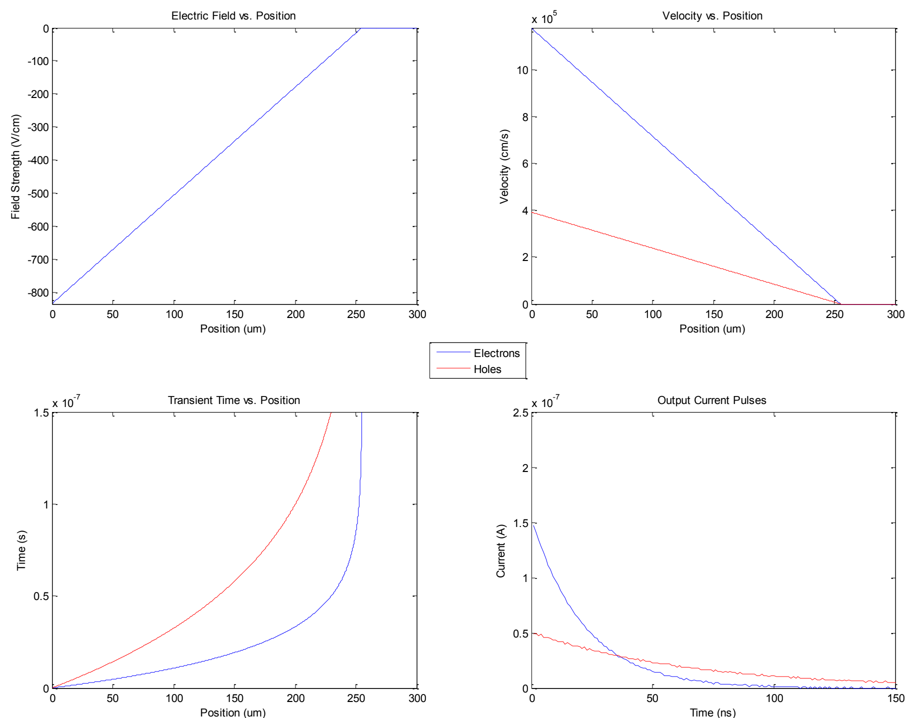


**Figure 4.5** The modeled parameters of the sensor when it is biased at -10V.

The plots very clearly show that as the bias is increased, the parameters governing the carrier behaviors are directly affected. When biased at -10V, the sensor is not yet fully depleted, which is shown by the plot of the electric field not reaching the full 300μm thickness. It can also be seen that at -10V, the velocities go to zero, and the transient times go to infinity in the region with no electric field.

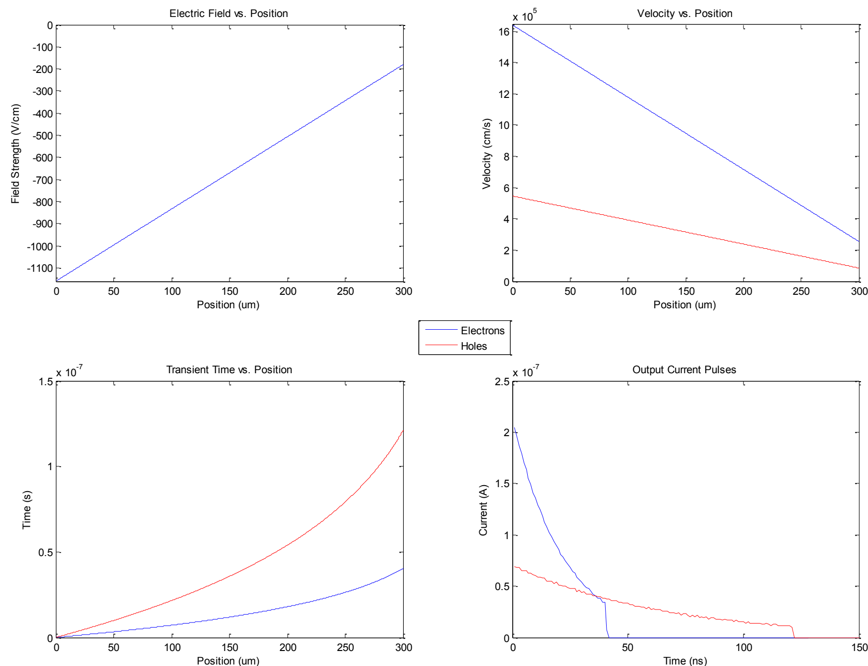


**Figure 4.6** The modeled parameters of the sensor when it is biased at -20V

When the magnitude of the bias is increased to -20V, the substrate has become fully depleted. The relationships between electric field, carrier velocity, and transient times are clearly evident. As a result of being fully depleted, a distinct pulse shape has emerged. This gives an insight into the magnitudes and durations that can be expected on the front and back side channels of the sensor when it is hit with radiation.

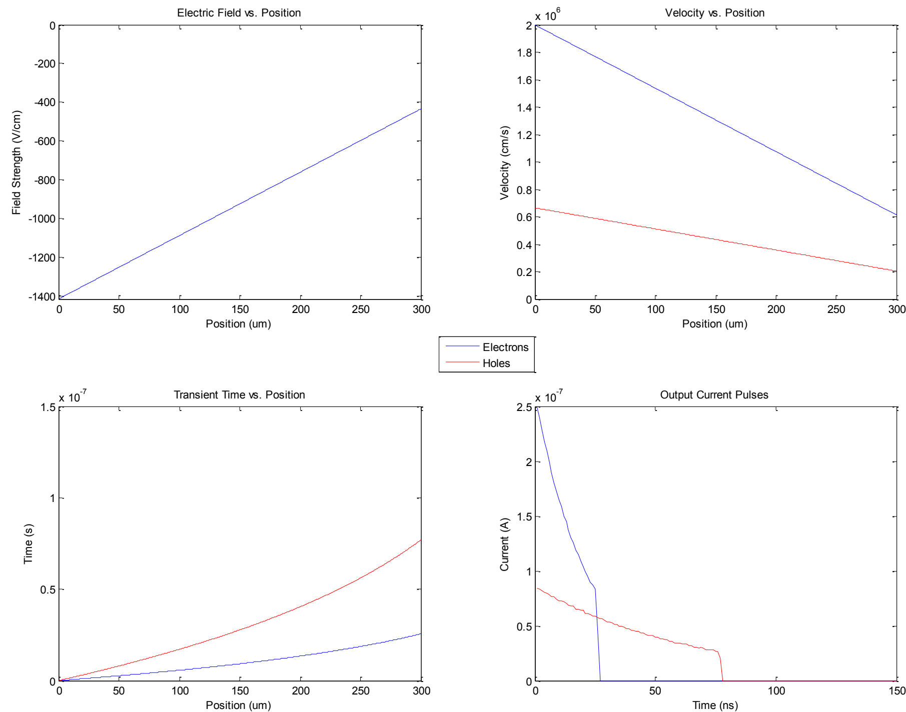


**Figure 4.7** The modeled parameters of the sensor when it is biased at -30V

As the biasing magnitude is increased further, the parameters continue to change. At -30V, the substrate is now over depleted, which means there are still no charge carriers present, but the magnitude of the electric field has increased. This has the effect of increasing the velocities, decreasing the transient times, and both increasing the magnitude, and decreasing the duration of the output current pulses. It is safe to assume that the sensor will perform better at higher biases. The main benefits are the increased velocity and decreased transient times. The charge is swept out faster, therefore, there is less opportunity for charge to recombine and be lost.

## Generation 4 Sensor Testing

This section will detail the testing set up and results of the generation 4 sensor. A comparison between the generation 3 sensor and the generation 4 sensor was necessary to gain an understanding of how well the generation 4 sensor may perform when in a radiation environment. The desire for this direct comparison necessitated that the generation 4 sensor be tested by the same metrics as the generation 3 sensor. These metrics, described in Chapter Two, were the inter-strip resistances and the voltage at each channel when the infrared laser was aimed at the sensor.

### Inter-Strip Resistance

The resistance between channel one and every other channel was measured on both the front and the back of the sensor. As with the third generation sensor, the generation 4 is sensitive to light, so the resistance measurement was taken with the sensor in complete darkness. The measurements can be found in Table G.1 in Appendix G. The results of the resistance test are very similar to the generation 3 sensor, with the exception that the front side of the generation 4 sensor looks similar to the back side of the generation 3 sensor, and the back side of the generation 4 sensor has similar resistances as the front side of the generation 3 sensor. This is a very odd result, and is not easily explained without more information on the physical parameters of the generation 3 sensor. One hypothesis is that the substrate used in the generation 3 sensor is more highly doped than the near intrinsic silicon used in the generation 4 sensor. This may account for

the difference, but without knowing this concentration, or any of the other concentrations, it is impossible to determine.

Results of Infrared Laser Stimulation

The generation 4 sensor was tested in a nearly identical manner to the generation 3 sensor as outlined in Chapter Two. A picture of the testing apparatus is presented in Figure 4.8.

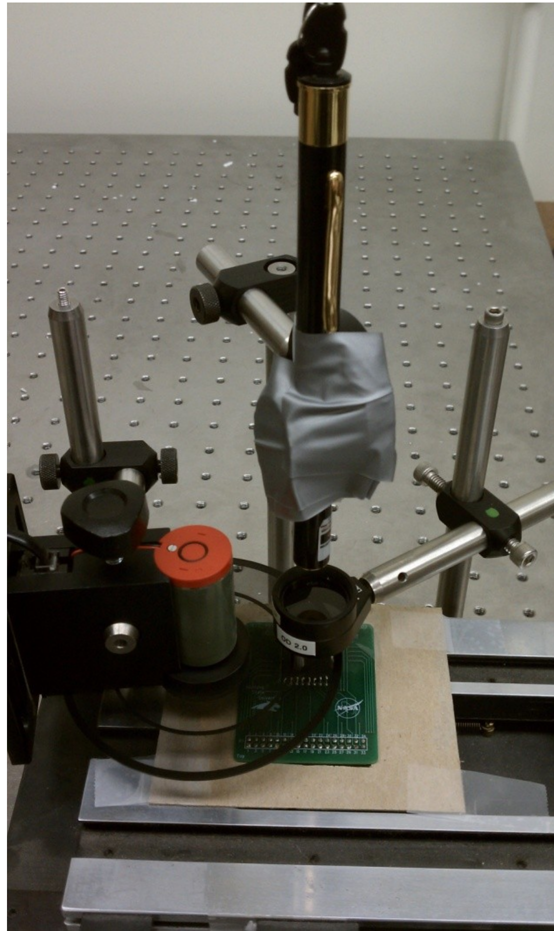


**Figure 4.8** A picture of the testing apparatus used. The packaged generation 4 sensor is on a X-Y translation stage to provide accurate positioning of the laser.

The laser was moved to five different positions on the sensor (the four corners, and the center), and measurements were taken from each channel at each position at a -10V, -20V, and -30V bias. The data collected is available in Tables G.2-G.6 in Appendix G. A picture of the laser's position, as illuminated by an IR-card is shown in Figure 4.9.

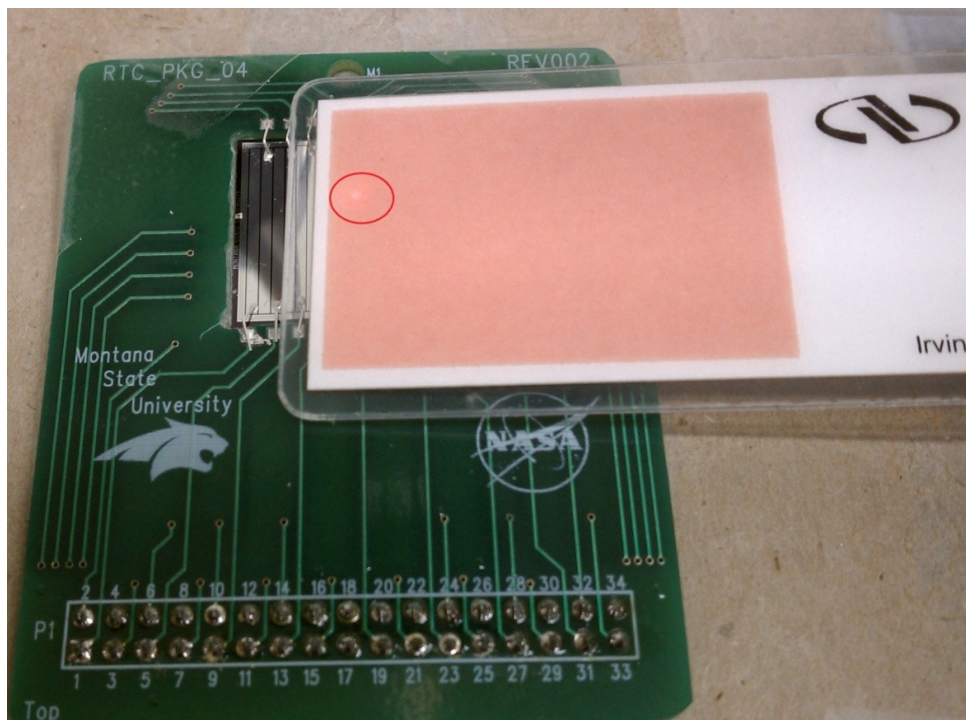


**Figure 4.9** The infrared lasers position as illustrated by an IR-card. The position is highlighted by the red circle

To create plots that are useful for comparison, the data taken was normalized in the same way as the generation 3 sensor's data. The lowest value was subtracted from all channels, as an attempt to minimize the effect of lateral diffusion, then each channel was divided by the larges measured value to give values ranging from 0 to 1. Unfortunately,

even with the data normalized, the sensor's response is still dominated by the effects of lateral diffusion.

The results of the infrared laser tests are shown in Figures 4.10-4.14. For each group of plots, the first column is the front side response, the second column is the back side response, and the third column is the combined response. Each row also indicates a different bias voltage with the top row at -10V, the middle at -20V, and the bottom at -30V.

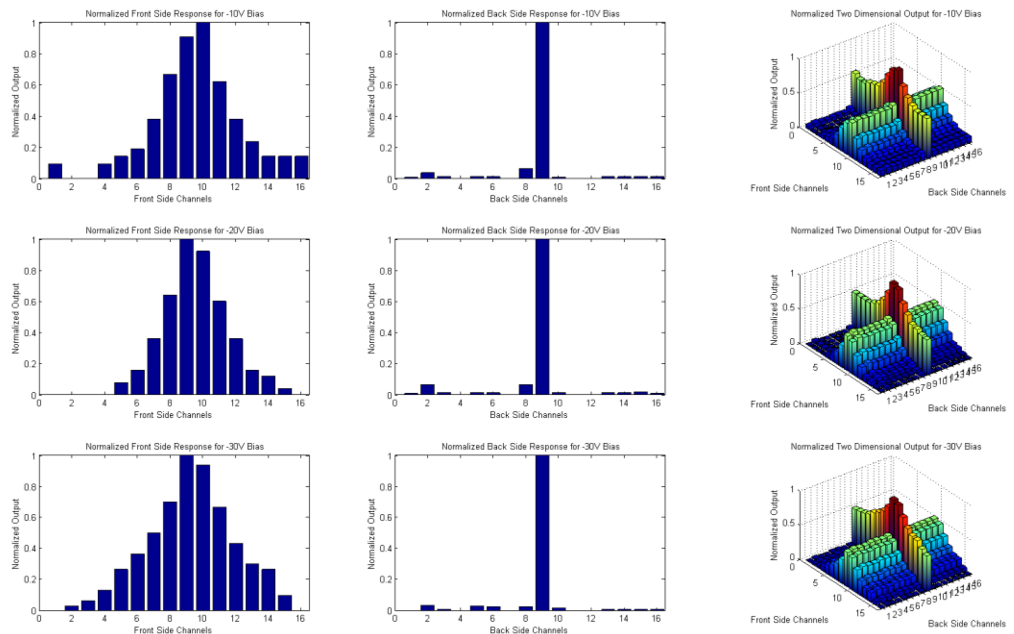


**Figure 4.10** The response of the generation 4 sensor when the laser is aimed at approximately the center of the sensor

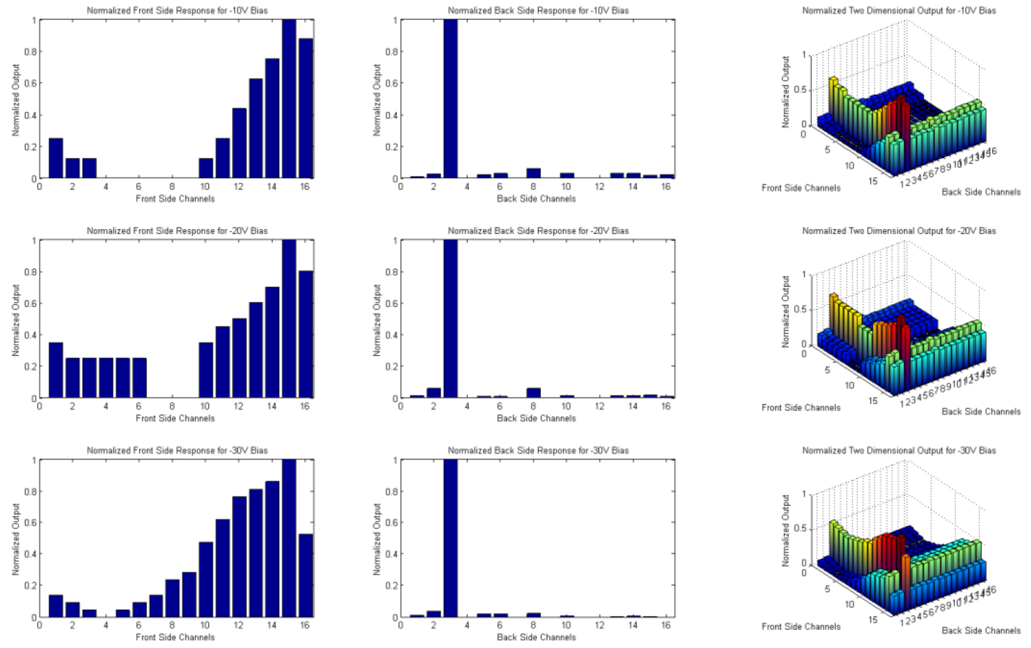


**Figure 4.11** The response of the generation 4 sensor when the laser is aimed at the lower-left corner of the sensor.

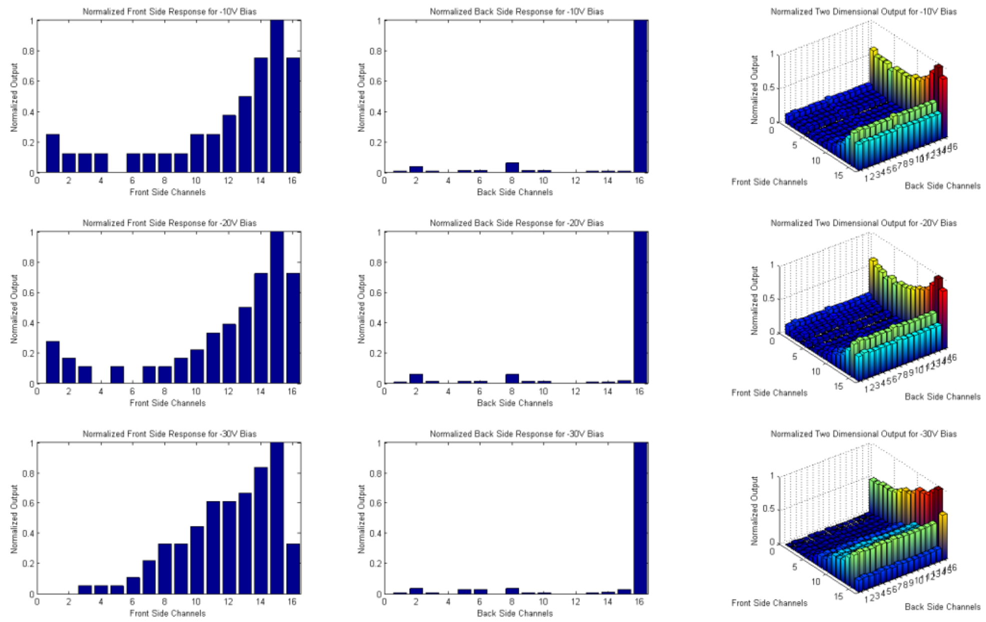


**Figure 4.12** The response of the generation 4 sensor when the laser is aimed at the lower-right corner of the sensor

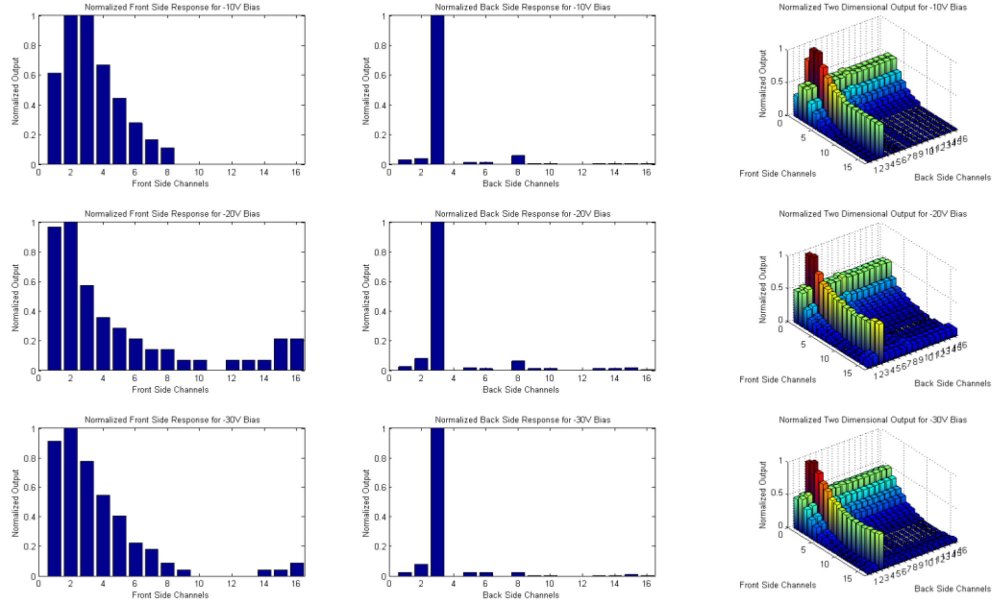


**Figure 4.13** The response of the generation 4 sensor when the laser is aimed at the upper-left corner of the sensor

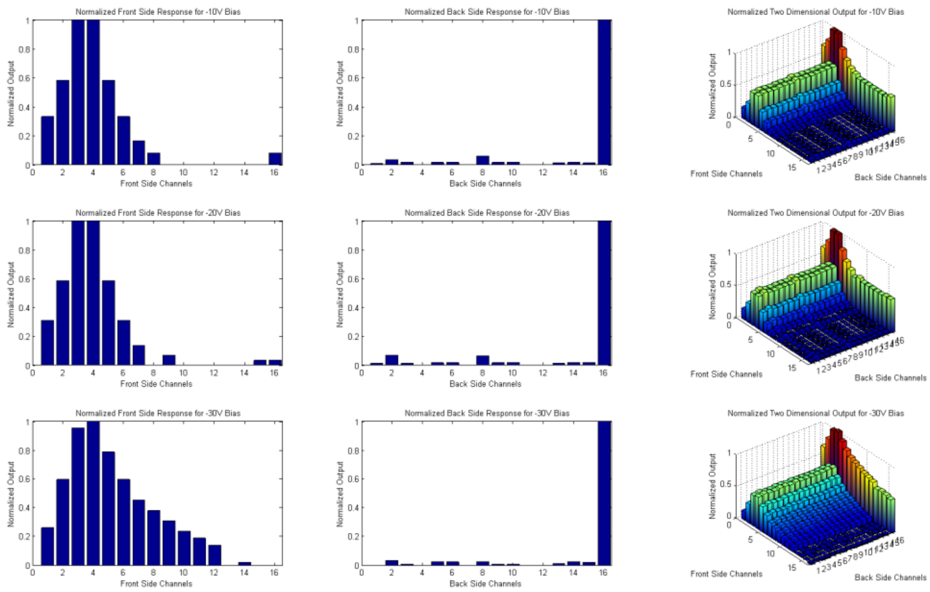


**Figure 4.14** The response of the generation 4 sensor when the laser is aimed at the upper-right corner of the sensor

While the plots of the generation 4 sensor data clearly indicate which area of the sensor is being hit, there is little obvious improvement in the performance when the gain is increased. The only noticeable improvement is the reduction of front side channels that are relatively distant from the area being excited by the laser. The effects of lateral diffusion due to the high concentration of EHPs created by the laser are dominating the front side response. The back side however, is largely unaffected by the lateral diffusion for two reasons. The first is that electrons have a much higher mobility, and a shorter transient time, so they are more likely to be collected quickly before they diffuse too far. The second, and more important reason, is that the back side contains the P+ barrier diffusions which act to isolate the N+ channels, and indeed aid in minimizing lateral diffusion. The front side has no such protection against diffusion, and if the plot shown in Figure 4.15, is extrapolated to the $10^{11}$ doping concentration of the generation 4 substrate, the hole diffusion length is on the order of 100cm.

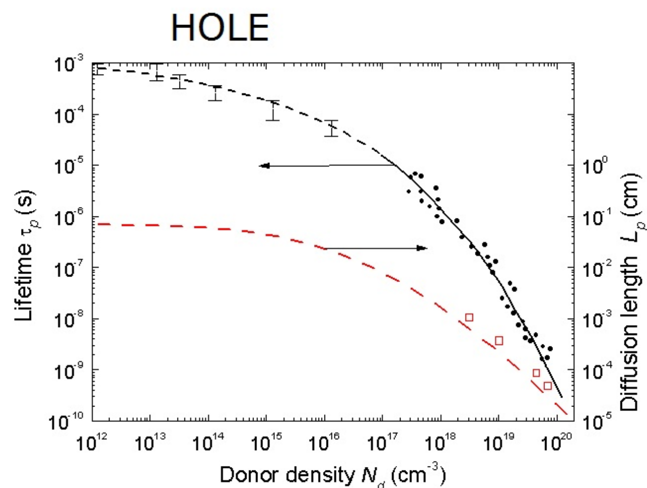


**Figure 4.15** A plot of experimentally obtained hole diffusion lengths and lifetimes vs. doping concentrations[7].

With the laser test, lateral diffusion of charge carriers is a definite problem as a result of the large carrier concentrations created by the laser. Both the generation 3 and the generation 4 sensors are affected by this phenomenon. The generation 4 sensor is more susceptible to the diffusion effects because, for one, it is smaller than the generation 3 sensor, so the carriers do not have to diffuse as far, and secondly, the doping of the generation 4 substrate is likely much less than the generation 3 substrate as discussed in the previous section.

By taking all of the inherent differences into account, the generation 4 sensor performs relatively well when compared to the generation 3 sensor. The real testing for understanding the capabilities of each sensor will need to be done using radioactive sources to produce ionizing radiation strikes, and testing the outputs produced.

## Design Improvements

Although the COMSOL and MATLAB simulation results and the physical testing results indicate that the sensors are effective for spatial detection of ionizing radiation, the complexity of the physics at work in the device make understanding and predicting their real world behavior exceedingly difficult.

### Two-Dimensional Multi-Channel Modeling

In order to better understand the complex processes at work inside the sensor, a more complex model must be developed. The current COMSOL models of the sensor's operation do not take into account the doping concentrations and corresponding electric fields of the implanted channels, let alone a series of them. Understanding of the sensor's

fundamental operation is extremely important, and a simulating the movement of charge distributions near the doped channels will advance that understanding tremendously.

### Non-Saturating Device Testing

As previously mentioned, testing of the sensors with a laser source produces far too much charge in the substrate to serve as an accurate representation of the device's performance radioactive environments. A testing procedure that uses a more controlled method of producing EHPs in the sensor substrate would be extremely beneficial in characterization.

Currently, the testing apparatus relies upon and always-on laser source pulsed by a chopper wheel. This does create a pulsed laser signal, but the laser illuminates the sensor for a period of time several orders of magnitude longer that a charge carrier's transient time across the width of the device, creating a dominating lateral diffusion effect.

A method that could apply a laser or other illumination source that could provide and extremely short burst of energy to the sensor would be ideal. Perhaps the use of a Xenon camera flash to create a burst of high-energy photons, used in conjunction with a shielding device to focus the light on a small area of the sensor would be an easy alternative.

## Conclusions

By accounting for the fact that the current laser-based testing apparatus creates too much charge in the sensor's substrate, it works as expected. The area excited by the

laser can be clearly seen. For the sensor to perform in a more predictable fashion, more work would need to be focused on modeling the physical processes at work in the sensor. Recommendations for future work and a summary of the project are discussed in Chapter Five.

# CHAPTER FIVE

# PROJECT SUMMARY AND RECOMMENDATIONS FOR FUTURE RESEARCH

## Summary

The motivation for this project has been to develop a sensor capable of spatially detecting radiation in two dimensions for use with space-bound reconfigurable computers. A previous sensor design has been evaluated for use in the project, but was found to be lacking in desired capabilities. A commercially available sensor was purchased and has had its capabilities tested. The sensor design known as a strip sensor has been studied in detail, and used in a new sensor design that fits with the constraints of the project. The strip sensor was simulated in COMSOL and MATLAB, fabricated on silicon wafers, performance tested, compared to the performance of the commercial sensor, and presented in this thesis.

The results from the fabrication and testing of the device indicate that it operates as expected, and would be a feasible sensor to integrate with a reconfigurable computing system.

## Recommendation for Future Research

There is a large amount of investigation that could be directed towards the sensor and yield improvements in understanding and functionality. First, an obvious area of future research is to performance test the sensor in a radioactive environment. This will give a better understanding of the capabilities and overall quality of the sensor.

An improved fabrication process would be well worth investigating. The doping concentrations of the channels and barrier diffusions have a large impact on performance. An investigation into these effects and optimizing the desired traits would be a substantial benefit to the sensor's performance.

Investigating alternative biasing schemes could aid performance as well. By attempting a split-biasing scheme (bias voltage on the front and back), the sensor could be fully depleted with lower bias voltages. This may be an advantage in the future when integrating the sensor with the reconfigurable computer set up as it will require a smaller power supply.

Finally, an investigation into the long-term stability of the device would be necessary. A study of the bias ring's performance would also be an integral part of this investigation. With a sensor system that is stable in its performance of the long-term, the system would be ready for deployment in a space-bound experiment.

# REFERENCES CITED

[1] "4.4 The Electrostatic Analysis of a P-n Diode." *Department of Electrical, Computer, and Energy Engineering (ECEE) | University of Colorado at Boulder*. Web. 25 Apr. 2011. <http://ecee.colorado.edu/~bart/book/pnelec.htm>.

[2] "File:Pn-junction-equilibrium.png." *Wikipedia, the Free Encyclopedia*. Web. 29 April 2011. <http://en.wikipedia.org/wiki/File:Pn-junction-equilibrium.png>.

[3] "ATLAS- Silicon Detector." *Particle Physics Department at RAL*. Web. 01 May 2011. <http://hepwww.rl.ac.uk/OpenDays97/Atlas_SCT_sidetector.htm>.

[4] "Optical Properties of Silicon | Pveducation.org." *Welcome to the Photovoltaic Education Network | Pveducation.org*. Web. 04 May 2011. <http://www.pveducation.org/pvcdrom/appendicies/optical-properties-of-silicon>.

[5] U.C. Bergmann, H.O.U. Fynbo, and O. Tengblad, “Use of Si strip detectors for low-energy particles in compact geometry,” Nuclear Instruments & Methods in Physics Research, Section A, Vol. 515, pp. 657-664 (2003).

[6] H. Dijkstra, and J. Libby, “Overview of silicon detectors,” Nuclear Instruments & Methods in Physics Research, Section A, Vol. 494 pp. 86-93 (2002).

[7] Stefano Meroli, “The Minority Carrier Lifetime in Silicon Wafer. Bulk and Surface Recombination process.” *Scientific Lectures*. Web. 04 May 2011. < http://meroli.web.cern.ch/meroli/Lecture_lifetime.html>.

[8] A. Bischoff, N. Findeis, D. Hauff, P. Holl, J. Kemmer, P. Klein, P. Lechner, G. Lutz, R. H. Righter, and L. Studer, “Breakdown protection and long-term stabilization for Si-detectors,” Nuclear Instruments & Methods in Physics Research, Section A, Vol. 326 pp. 27-37 (1993).

[9] "Properties of Silicon - El-Cat.com." *Silicon Wafers & Ingots, III-V Substrates, Indium Phosphide, Electronic Materials - El-Cat.com*. Web. 06 May 2011. <http://www.el-cat.com/silicon-properties.htm>.

[10] Jaeger, Richard C. *Introduction to Microelectronic Fabrication*. Upper Saddle River, NJ: Prentice Hall, 2002. Print.

# APPENDICES

# APPENDIX A

## GENERATION 1 SENSOR RESPONSE PLOTS

Note: This is the measured data from a typical generation 1 single-sided sensor. There is no data for when the laser is aimed at channel 3.

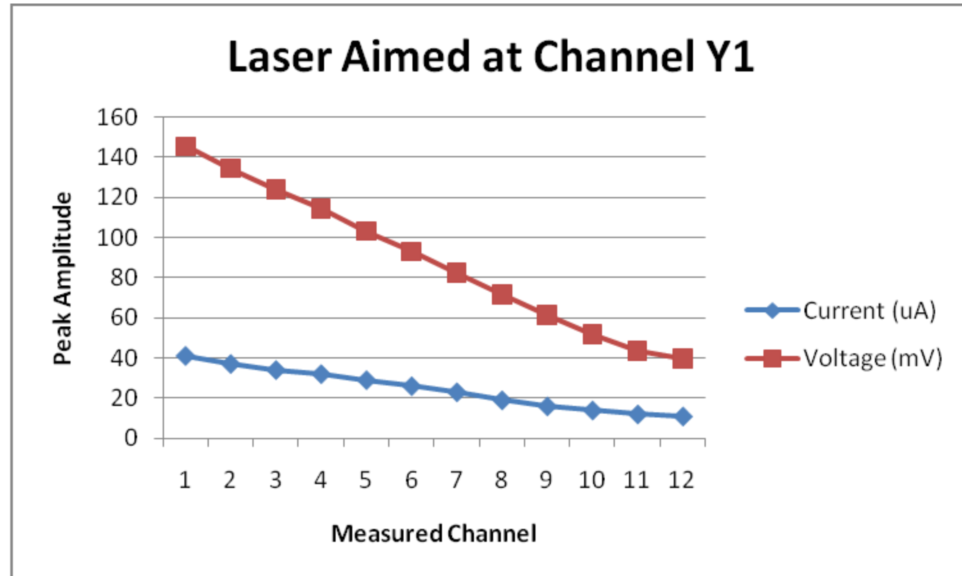


**Figure A.1** Each channel's response when the laser is aimed at the top channel

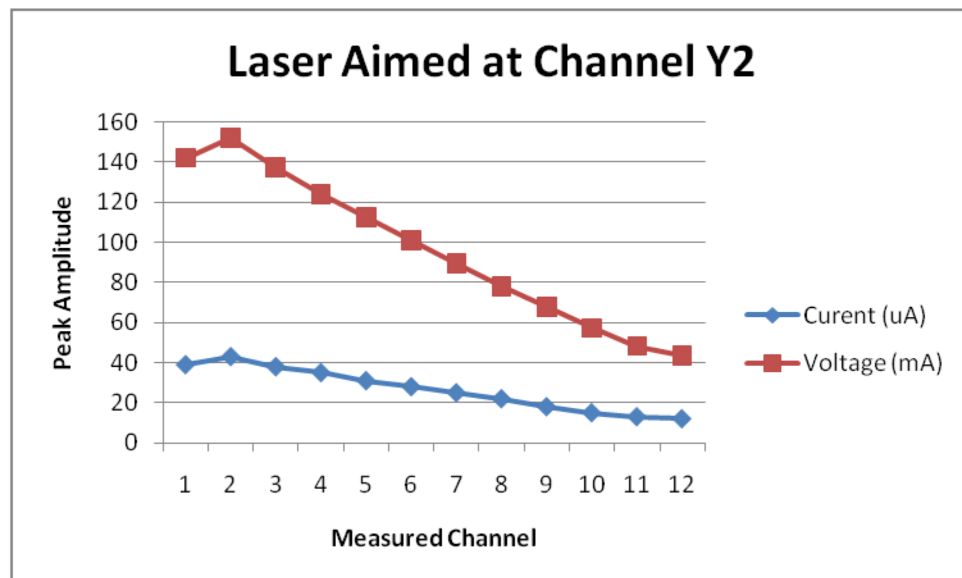


**Figure A.2** Each channel's response when the laser is aimed at channel 2

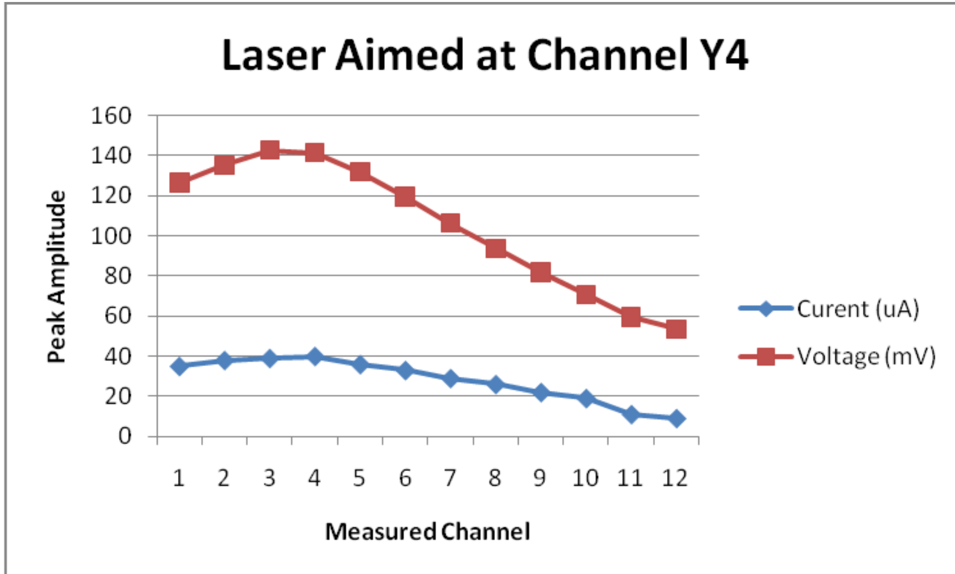


**Figure A.3** Each channel's response when the laser is aimed at channel 4

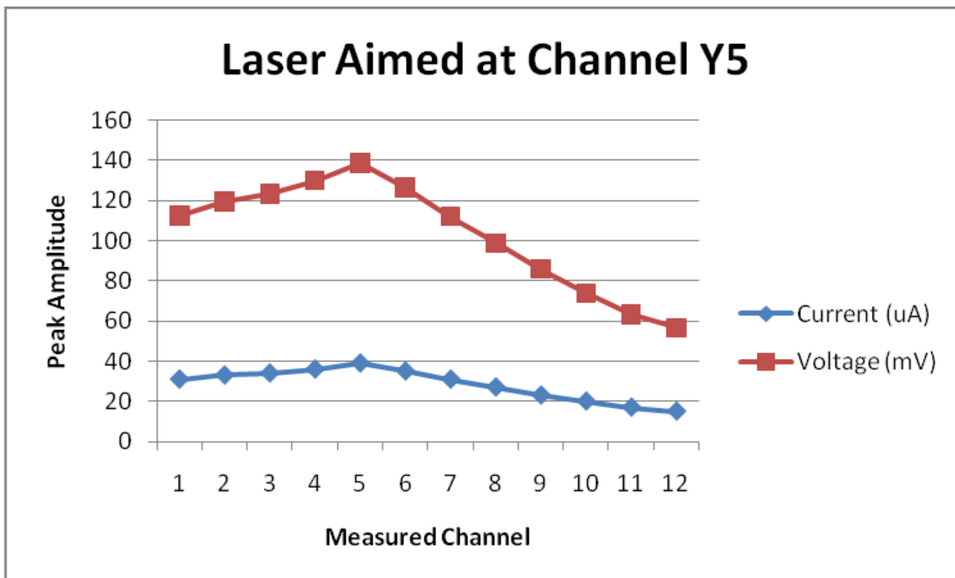


**Figure A.4** Each channels response when the laser is aimed at channel 5

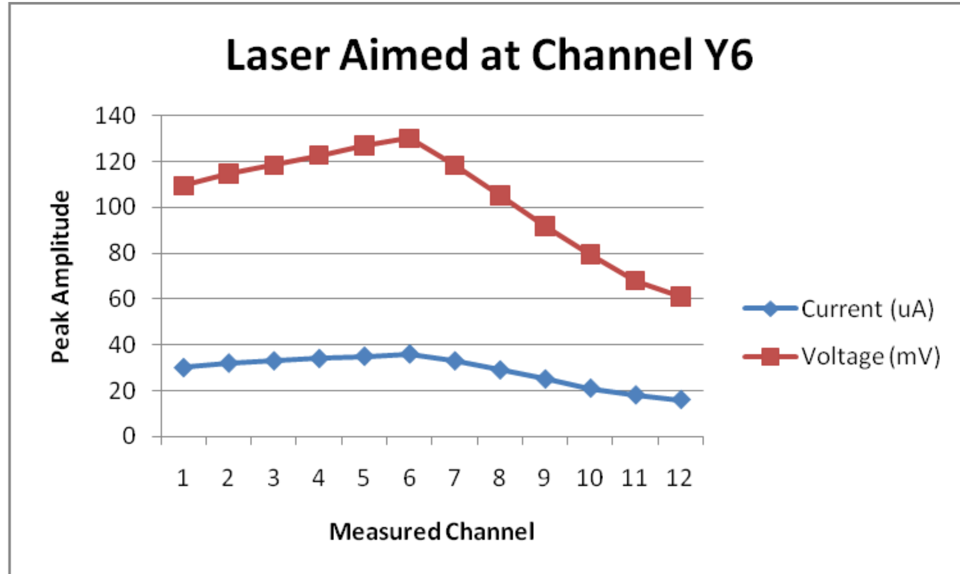


**Figure A.5** Each channel's response when the laser is aimed at channel 6

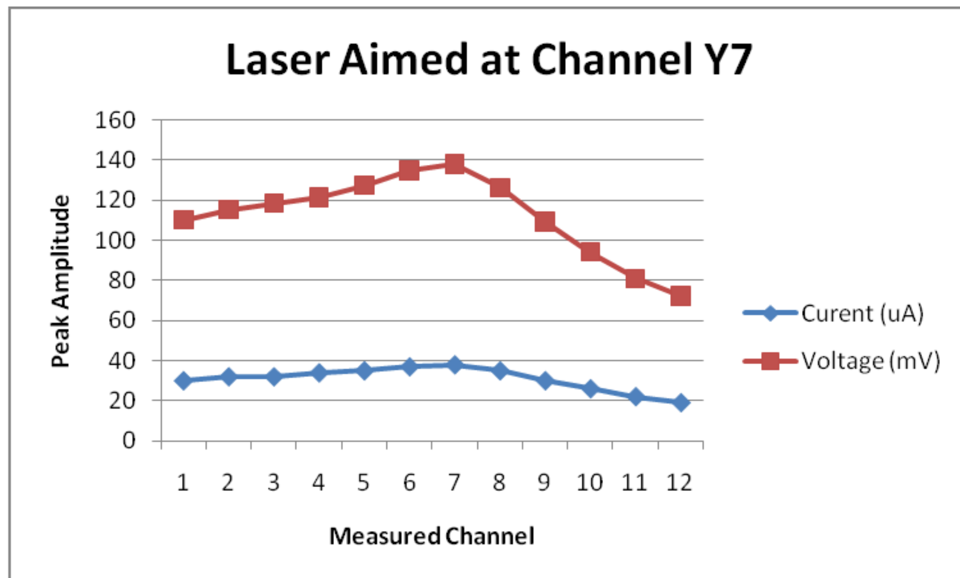


**Figure A.6** Each channel's response when the laser is aimed at channel 7

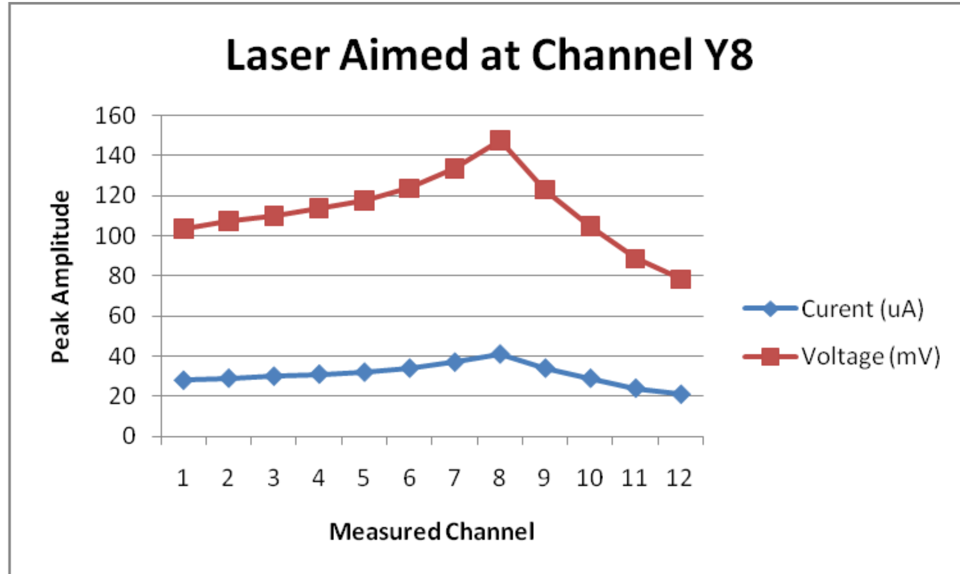


**Figure A.7** Each channel's response when the laser is aimed at channel 8

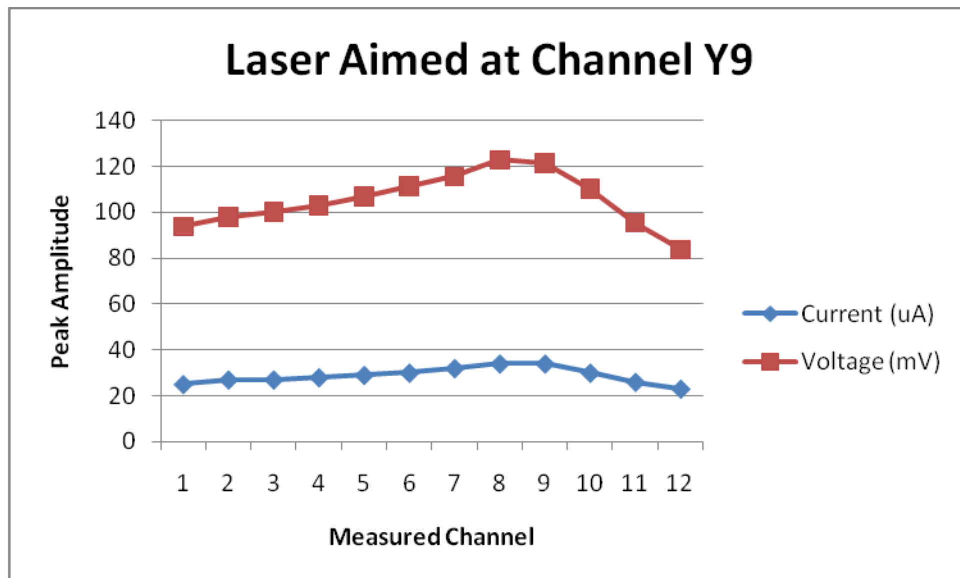


**Figure A.8** Each channel's response when the laser is aimed at channel 9

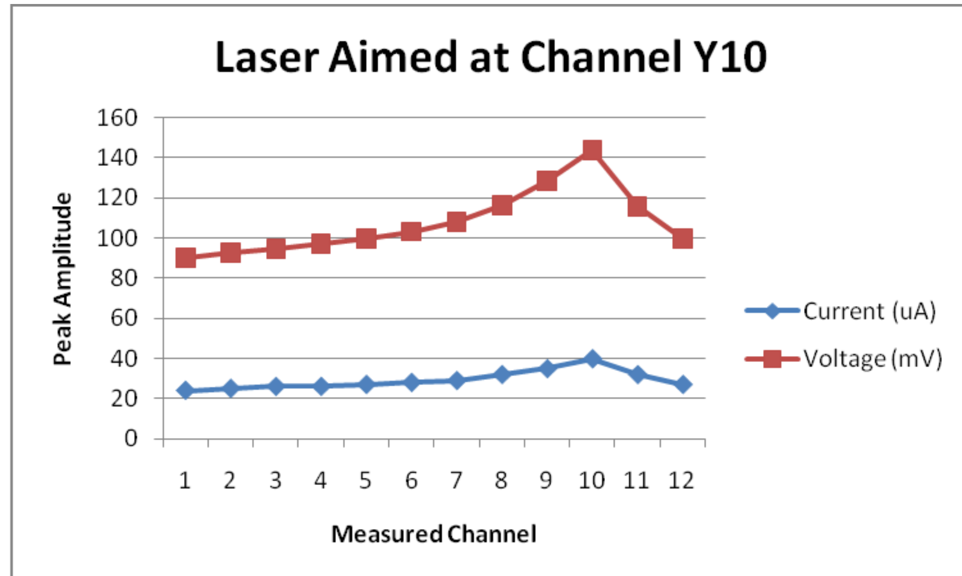


**Figure A.9** Each channel's response when the laser is aimed at channel 10

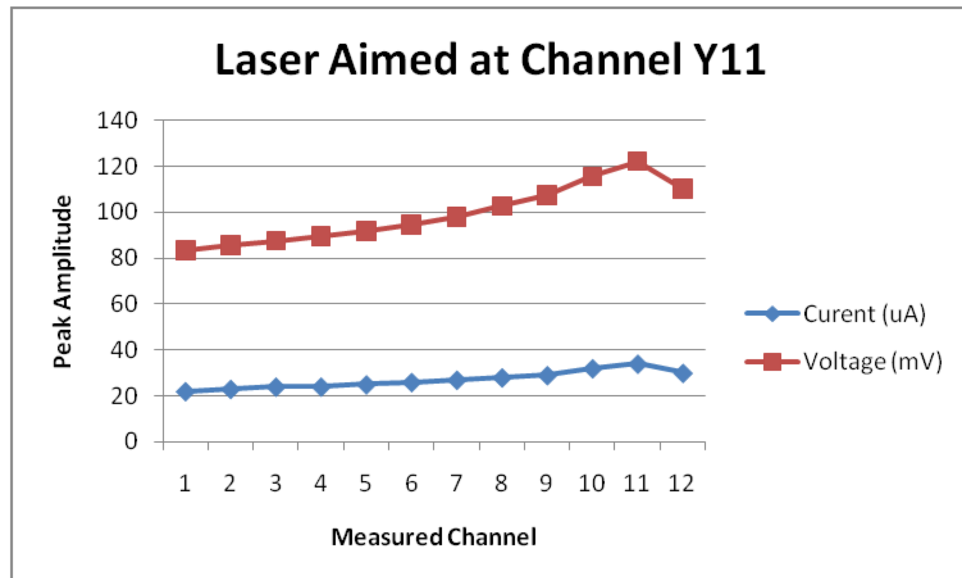


**Figure A.10** Each channel's response when the laser is aimed at channel 11

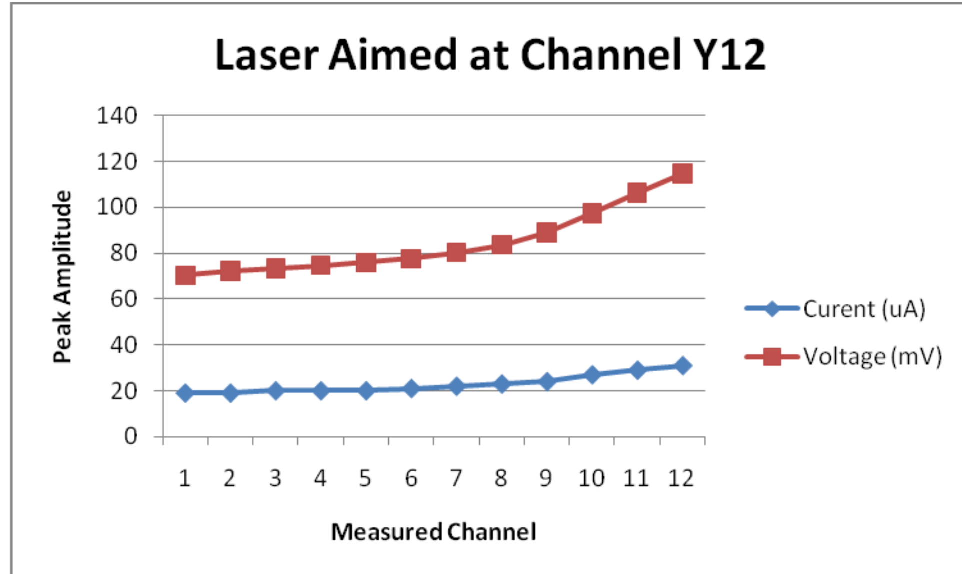


**Figure A.11** Each channel’s response when the laser is aimed at channel 12

# APPENDIX B

## GENERATION 3 SENSOR MEASURED DATA

**Table B.1** Generation 3 sensor inter-strip resistance

| Channel | Resistance (Ω) |
|---|---|
| **F-1 to F-2** | ∞ |
| **F-1 to F-3** | ∞ |
| **F-1 to F-4** | ∞ |
| **F-1 to F-5** | ∞ |
| **F-1 to F-6** | ∞ |
| **F-1 to F-7** | ∞ |
| **F-1 to F-8** | ∞ |
| **F-1 to F-9** | ∞ |
| **F-1 to F-10** | ∞ |
| **F-1 to F-11** | ∞ |
| **F-1 to F-12** | ∞ |
| **F-1 to F-13** | ∞ |
| **F-1 to F-14** | ∞ |
| **F-1 to F-15** | ∞ |
| **F-1 to F-16** | ∞ |
| **B-1 to B-2** | 3.02K |
| **B-1 to B-3** | 4.86K |
| **B-1 to B-4** | 5.96K |
| **B-1 to B-5** | 6.61K |
| **B-1 to B-6** | 7.03K |
| **B-1 to B-7** | 7.30K |
| **B-1 to B-8** | 7.53K |
| **B-1 to B-9** | 7.68K |
| **B-1 to B-10** | 7.80K |
| **B-1 to B-11** | 7.87K |
| **B-1 to B-12** | 7.90K |
| **B-1 to B-13** | 7.84K |
| **B-1 to B-14** | 7.64K |
| **B-1 to B-15** | 7.07K |
| **B-1 to B-16** | 5.77K |

**Table B.2** Generation 3 sensor output at -10V, -20V, and -30V bias

| Channel | -10 V Bias (V) | -20 V Bias (V) | -30 V Bias (V) |
|---|---|---|---|
| **F-1** | -0.100 | -0.100 | -0.100 |
| **F-2** | -0.100 | -0.100 | -0.100 |
| **F-3** | -0.100 | -0.100 | -0.100 |
| **F-4** | -0.050 | -0.050 | -0.100 |
| **F-5** | -4.60 | -3.26 | -3.29 |
| **F-6** | -4.30 | -3.20 | -3.23 |
| **F-7** | -0.050 | -0.050 | -0.050 |
| **F-8** | -0.100 | -0.100 | -0.100 |
| **F-9** | -0.100 | -0.100 | -0.100 |
| **F-10** | -0.100 | -0.100 | -0.100 |
| **F-11** | -0.100 | -0.100 | -0.100 |
| **F-12** | -0.100 | -0.100 | -0.100 |
| **F-13** | -0.100 | -0.100 | -0.100 |
| **F-14** | -0.100 | -0.100 | -0.100 |
| **F-15** | -0.100 | -0.100 | -0.100 |
| **F-16** | -0.100 | -0.150 | -0.100 |
| **B-1** | 0.490 | 0.570 | 0.830 |
| **B-2** | 0.480 | 0.340 | 0.100 |
| **B-3** | 0.480 | 0.240 | 0.075 |
| **B-4** | 0.480 | 0.230 | 0.230 |
| **B-5** | 0.490 | 0.200 | 0.400 |
| **B-6** | 0.500 | 0.324 | 0.300 |
| **B-7** | 0.510 | 0.710 | 0.340 |
| **B-8** | 0.525 | 1.32 | 3.84 |
| **B-9** | 0.510 | 0.750 | 0.540 |
| **B-10** | 0.490 | 0.370 | 0.050 |
| **B-11** | 0.475 | 0.270 | 0.050 |
| **B-12** | 0.475 | 0.270 | 0.050 |
| **B-13** | 0.465 | 0.340 | 0.100 |
| **B-14** | 0.465 | 0.340 | 0.100 |
| **B-15** | 0.470 | 0.280 | 0.100 |
| **B-16** | 0.470 | 0.580 | 0.900 |

# APPENDIX C

## MASK SET PHOTOGRAPHS

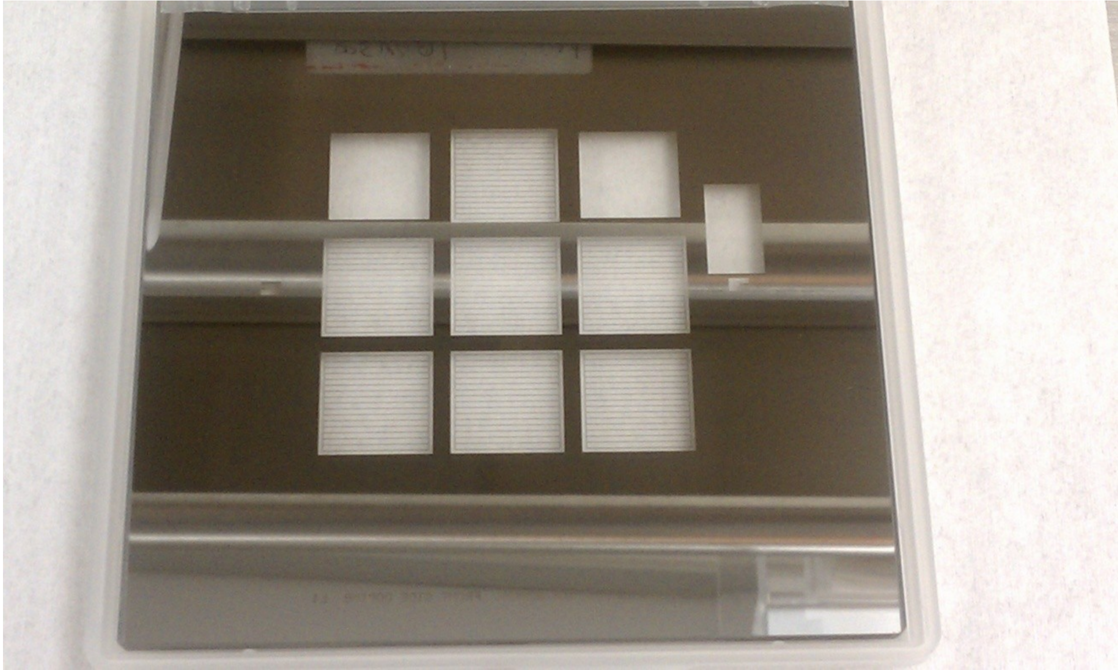

**Figure C.1** A picture of Mask #1. The front side P+ channels

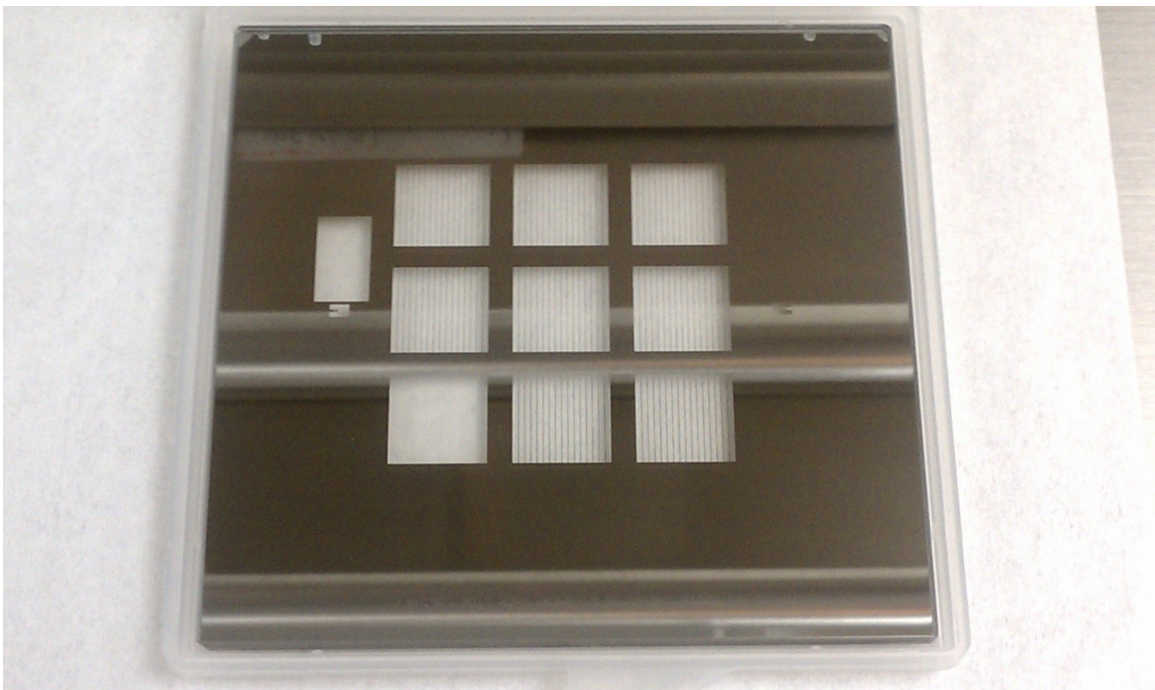

**Figure C.2** A picture of Mask #2. The back side N+ channels

**Figure C.3** A picture of Mask #3. The back side P+ barriers

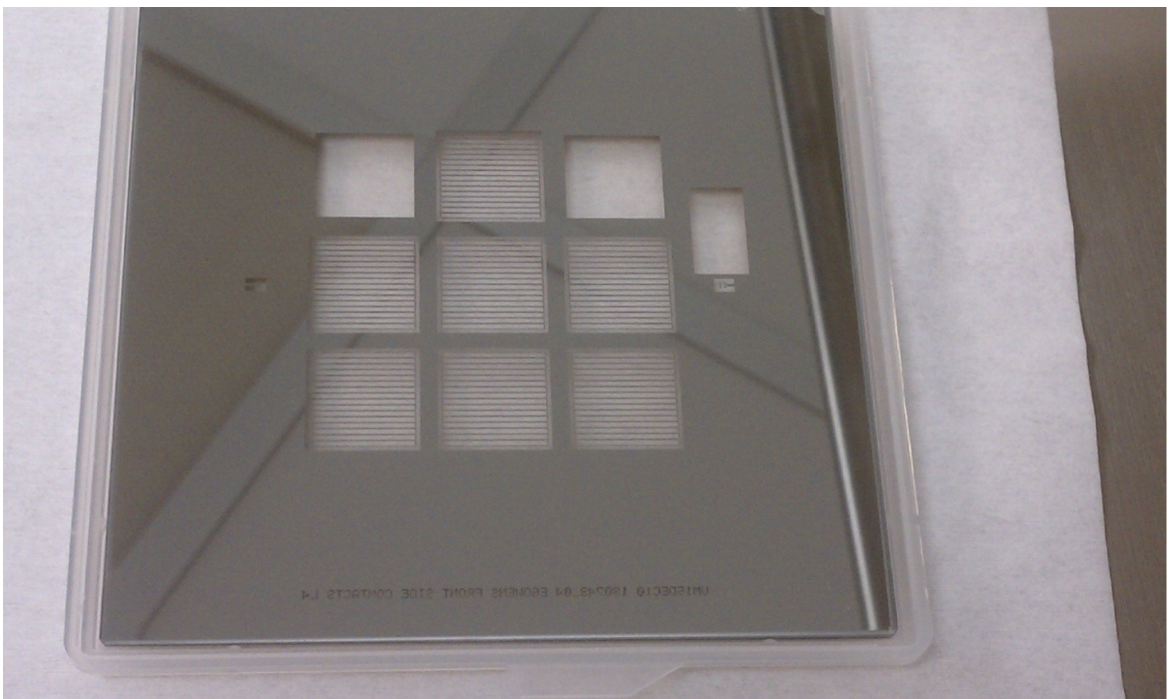

**Figure C.4** A picture of Mask #4. The front side contacts

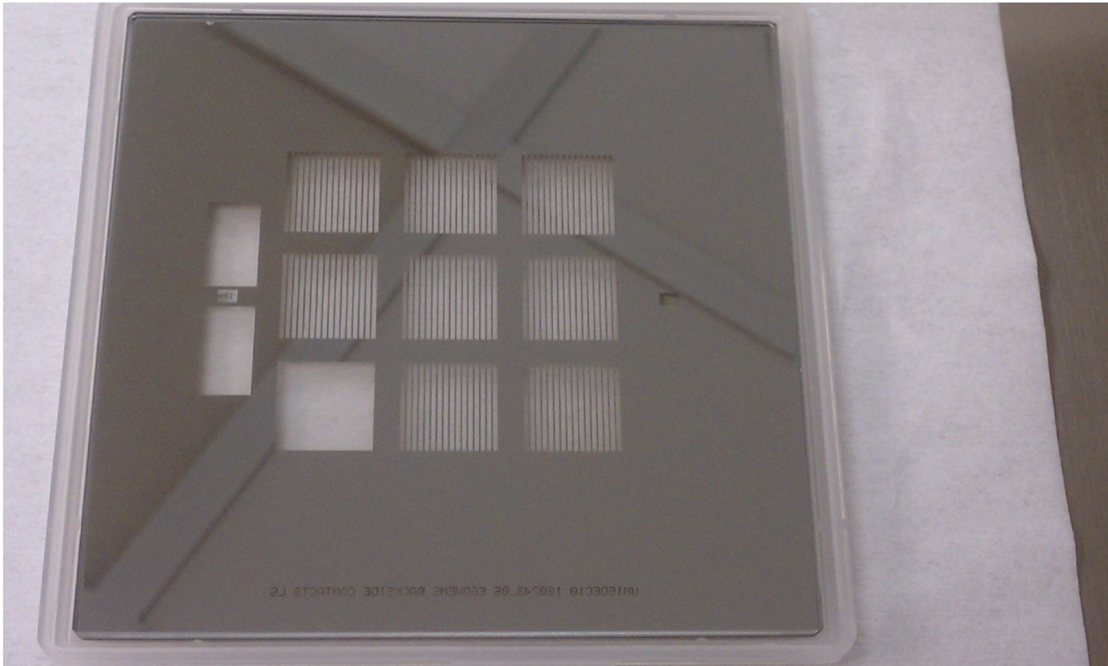

**Figure C.5** A picture of Mask #5. The back side contacts

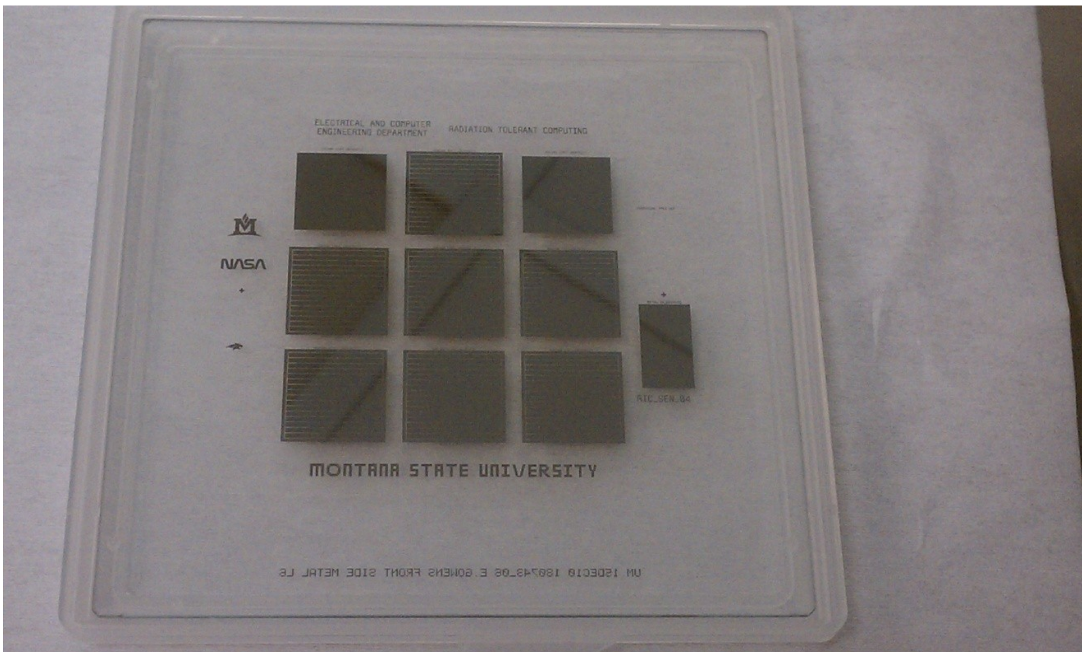


**Figure C.6** A picture of Mask #6. The front side metal

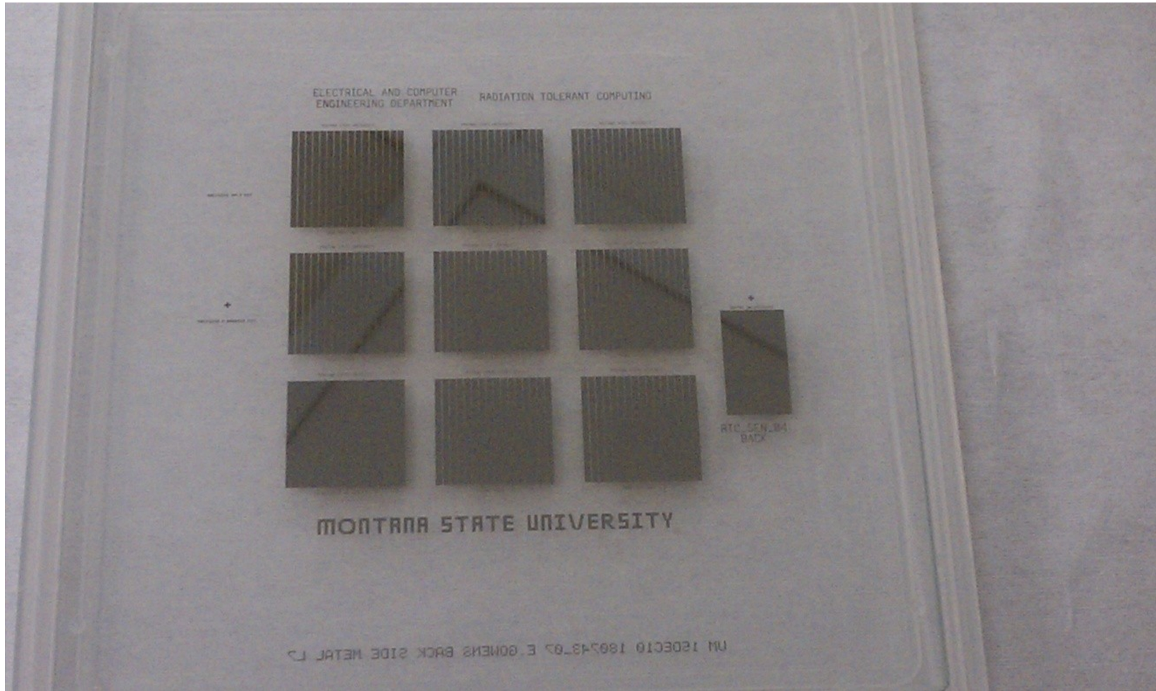


**Figure C.7** A picture of Mask #7. The back side metal

# APPENDIX D

# FABRICATION SEQUENCE

1. Oxidation (Front Side P+ Channels)
    a. Temperature 1000° C
    b. Time 90 min
    c. Wet/Dry Wet
    d. Nitrogen Flow 7
    e. Oxygen Flow 9
2. Photolithography for P+ Channels
    a. Photoresist S-1813
    b. Side To Spin Both
    c. Spin Program #9 (5250rpm for 30sec)
    d. Softbake Program #9 (115° C for 60sec)
    e. Mask #1
    f. Alignment Top Side
    g. Side to Pattern Front
    h. Exposure time 4.5sec
    i. Developer MF-319
    j. Developing Time 60sec
    k. Hardbake Program #9 (115° C for 60sec)
3. Oxide Etch
    a. Etchant 6:1 BOE
    b. Etch Rate 900Å/min
    c. Etch Time ~6min
4. Solvent Clean
    a. Rinse with Acetone
    b. Rinse with Isopropanol
    c. Rinse with Methanol
    d. Rinse with DI water and Dry
5. RCA Clean
    a. Soak 1 Piranha Etch (3:1 $H_2O_2$:$H_2SO_4$)
    b. Soak 1 Temp Room Temperature
    c. Soak 1 Time 10min
    d. DI Water Rinse 2min
    e. Soak 2 HF Dip (6:1 BOE ok too)
    f. Soak 2 Time 15 sec
    g. DI Water Rinse 30sec
    h. Soak 3 Ionic Clean (6:1:1 $H_2O$:$H_2O_2$:HCl)
    i. Soak 3 Temp 40° C
    j. Soak 3 Time 10min
    k. DI Water Rinse 5min

6. Front Side P+ Diffusion
    a. Furnace — Boron
    b. Sources — Boron- 1source/2 wafers
    c. Side Facing Sources — Front
    d. Temperature — 950° C
    e. Time — 60min
    f. Nitrogen Flow — 7
7. BSG Etch
    a. Etchant — 6:1 BOE
    b. Time — 10-15min (visual inspection)
    c. DI Water Rinse — 5min
8. Oxidation (Back Side N+ Channels)
    a. Temperature — 1000° C
    b. Time — 90 min
    c. Wet/Dry — Wet
    d. Nitrogen Flow — 7
    e. Oxygen Flow — 9
9. Aluminum Deposition
    a. Side for Deposition — Front
    b. Desired Thickness — ~300nm
    c. Amount of Al to Use — ~130cm$^2$ for 4 wafers (PVD)
10. Photolithography for Back Side Alignment
    a. Photoresist — S-1813
    b. Side To Spin — Front
    c. Spin Program — #9 (5250rpm for 30sec)
    d. Softbake Program — #9 (115° C for 60sec)
    e. Mask — #1
    f. Alignment — Top Side
    g. Side to Pattern — Front
    h. Exposure time — 4.5sec
    i. Developer — MF-319
    j. Developing Time — 60sec
    k. Hardbake Program — #9 (115° C for 60sec)
11. Aluminum Etch
    a. Etchant — Aluminum Etch
    b. Temperature — 70° C
    c. Time — ~5min (visual inspection)
    d. DI Water Rinse — By hand
12. Solvent Clean
    a. Rinse with Acetone
    b. Rinse with Isopropanol
    c. Rinse with Methanol
    d. Rinse with DI water and Dry

13. Photolithography for N+ Channels
    a. Photoresist S-1813
    b. Side To Spin Both
    c. Spin Program #9 (5250rpm for 30sec)
    d. Softbake Program #9 (115° C for 60sec)
    e. Mask #2
    f. Alignment Back Side
    g. Side to Pattern Front
    h. Exposure time 4.5sec
    i. Developer MF-319
    j. Developing Time 60sec
    k. Hardbake Program #9 (115° C for 60sec)
14. Oxide Etch
    a. Etchant 6:1 BOE
    b. Etch Rate 900Å/min
    c. Etch Time ~6min
15. Solvent Clean
    a. Rinse with Acetone
    b. Rinse with Isopropanol
    c. Rinse with Methanol
    d. Rinse with DI water and Dry
16. Aluminum Etch
    a. Etchant Aluminum Etch
    b. Temperature 70° C
    c. Time ~5min (visual inspection)
    d. DI Water Rinse By hand
17. RCA Clean
    a. Soak 1 Piranha Etch (3:1 $H_2O_2$:$H_2SO_4$)
    b. Soak 1 Temp Room Temperature
    c. Soak 1 Time 10min
    d. DI Water Rinse 2min
    e. Soak 2 HF Dip (6:1 BOE ok too)
    f. Soak 2 Time 15 sec
    g. DI Water Rinse 30sec
    h. Soak 3 Ionic Clean (6:1:1 $H_2O$:$H_2O_2$:HCl)
    i. Soak 3 Temp 40° C
    j. Soak 3 Time 10min
    k. DI Water Rinse 5min

18. Back Side N+ Diffusion
    a. Furnace — Phosphorus
    b. Sources — Phosphorus- 1source/2 wafers
    c. Side Facing Sources — Back
    d. Temperature — 950° C
    e. Time — 30min
    f. Nitrogen Flow — 7
19. PSG Etch
    a. Etchant — 6:1 BOE
    b. Time — 5-10min (visual inspection)
    c. DI Water Rinse — 5min
20. Oxidation (P+ Barriers)
    a. Temperature — 1000° C
    b. Time — 90 min
    c. Wet/Dry — Wet
    d. Nitrogen Flow — 7
    e. Oxygen Flow — 9
21. Photolithography for P+ Barriers
    a. Photoresist — S-1813
    b. Side To Spin — Both
    c. Spin Program — #9 (5250rpm for 30sec)
    d. Softbake Program — #9 (115° C for 60sec)
    e. Mask — #3
    f. Alignment — Top Side
    g. Side to Pattern — Back
    h. Exposure time — 4.5sec
    i. Developer — MF-319
    j. Developing Time — 60sec
    k. Hardbake Program — #9 (115° C for 60sec)
22. Oxide Etch
    a. Etchant — 6:1 BOE
    b. Etch Rate — 900Å/min
    c. Etch Time — ~6min
23. Solvent Clean
    a. Rinse with Acetone
    b. Rinse with Isopropanol
    c. Rinse with Methanol
    d. Rinse with DI water and Dry

24. RCA Clean
    a. Soak 1 — Piranha Etch (3:1 $H_2O_2$:$H_2SO_4$)
    b. Soak 1 Temp — Room Temperature
    c. Soak 1 Time — 10min
    d. DI Water Rinse — 2min
    e. Soak 2 — HF Dip (6:1 BOE ok too)
    f. Soak 2 Time — 15 sec
    g. DI Water Rinse — 30sec
    h. Soak 3 — Ionic Clean (6:1:1 $H_2O$:$H_2O_2$:HCl)
    i. Soak 3 Temp — 40° C
    j. Soak 3 Time — 10min
    k. DI Water Rinse — 5min
25. Back Side P+ Barrier Diffusion
    a. Furnace — Boron
    b. Sources — Boron- 1source/2 wafers
    c. Side Facing Sources — Front
    d. Temperature — 950° C
    e. Time — 30min
    f. Nitrogen Flow — 7
26. BSG Etch
    a. Etchant — 6:1 BOE
    b. Time — 10-15min (visual inspection)
    c. DI Water Rinse — 5min
27. Oxidation (Contacts)
    a. Temperature — 1000° C
    b. Time — 60 min
    c. Wet/Dry — Dry
    d. Nitrogen Flow — 7
    e. Oxygen Flow — 9
28. Photolithography for Front Side Contacts
    a. Photoresist — S-1813
    b. Side To Spin — Both
    c. Spin Program — #9 (5250rpm for 30sec)
    d. Softbake Program — #9 (115° C for 60sec)
    e. Mask — #4
    f. Alignment — Top Side
    g. Side to Pattern — Front
    h. Exposure time — 4.5sec

29. Photolithography for Back Side Contacts
    a. Mask #5
    b. Alignment Top Side
    c. Side to Pattern Back
    d. Exposure time 4.5sec
    e. Developer MF-319
    f. Developing Time 60sec
    g. Hardbake Program #9 (115° C for 60sec)
        i. Note: Do steps 28 and 29 at the same time
30. Oxide Etch
    a. Etchant 6:1 BOE
    b. Etch Rate 900Å/min
    c. Etch Time ~1.5min
31. Solvent Clean
    a. Rinse with Acetone
    b. Rinse with Isopropanol
    c. Rinse with Methanol
    d. Rinse with DI water and Dry
32. Aluminum Deposition
    a. Side for Deposition Front
    b. Desired Thickness ~300nm-500nm
    c. Amount of Al to Use ~130cm$^2$ for 4 wafers (PVD)
33. Aluminum Deposition
    a. Side for Deposition Back
    b. Desired Thickness ~300nm-500nm
    c. Amount of Al to Use ~130cm$^2$ for 4 wafers (PVD)
34. Photolithography for Front Side Metal
    a. Photoresist S-1813
    b. Side To Spin Both
    c. Spin Program #9 (5250rpm for 30sec)
    d. Softbake Program #9 (115° C for 60sec)
    e. Mask #6
    f. Alignment Top Side
    g. Side to Pattern Front
    h. Exposure time 4.5sec
35. Photolithography for Back Side Metal
    a. Mask #7
    b. Alignment Top Side
    c. Side to Pattern Back
    d. Exposure time 4.5sec
    e. Developer MF-319
    f. Developing Time 60sec
    g. Hardbake Program #9 (115° C for 60sec)
        i. Note: Do steps 34 and 35 at the same time

36. Aluminum Etch
    a. Etchant — Aluminum Etch
    b. Temperature — 70° C
    c. Time — ~5min (visual inspection)
    d. DI Water Rinse — By hand
37. Solvent Clean
    a. Rinse with Acetone
    b. Rinse with Isopropanol
    c. Rinse with Methanol
    d. Rinse with DI water and Dry
38. Anneal
    a. Furnace — Boron
    b. Temperature — 400° C
    c. Time — 30min
    d. Nitrogen Flow — 7

# APPENDIX E

## CALCULATIONS OF GENERATION 4 SENSOR PARAMETERS

| **Fron Side P+ Channels** | Symbols | Value | Units | Notes |
|---|---|---|---|---|
| Boltzmann's Constant | k | 8.62E-05 | eV/K | |
| Background Concentration | $N_D$ | 2.15E+11 | Atoms/cm$^3$ | From El-Cat Website-Donor Concentration |
| **Frontside P+ (Original Doping)** | | | | First Diffusion |
| Temperature (deg C) | $T_c$ | 950 | C | |
| Temperature (K) | T | 1223 | K | deg C + 273 |
| Time (min) | $t_m$ | 60 | min | |
| Time(sec) | t | 3600 | sec | min*60 |
| Surface Concentration | $N_o$ | 1.20E+20 | Atoms/cm3 | [9], Figure 4.6 |
| Diffusion Coefficient Constant | $D_o$ | 10.5 | cm$^2$/sec | [9], Table 4.1 |
| Diffusion Coefficient Constant | $E_A$ | 3.69 | eV | [9], Table 4.1 |
| Diffusion Coefficient (Original) | $D_i$ | 6.61E-15 | cm$^2$/sec | $D = D_o*exp(-E_A/kT)$ |
| Dose | Q | 6.60E+14 | cm$^2$/sec | $Q=2*N_o*sqrt(D*t/pi)$ |
| Value of Functions | $N_D/N_o$ | 1.79E-09 | | |
| Inverse erfc | erfc$^{-1}$ | 4.26 | | http://fabweb.ece.uiuc.edu/utilities/erfc/default.aspx |
| Initial Junction Depth | $x_{ji}$ | 0.416 | um | $x_{ji} = 2*sqrt(D_i*t)*erfc^{-1}$ (cm) |
| **Drive in-Oxide 2** | | | | Oxide Growth for Patterning Backside Channels |
| Temperature (deg C) | $T_c$ | 1000 | C | |
| Temperature (K) | T | 1273 | K | deg C + 273 |
| Time (min) | $t_m$ | 90 | min | |
| Time (sec) | t | 5400 | sec | min*60 |
| Diffusion Coefficient (2nd) | $D_2$ | 2.61E-14 | cm$^2$/sec | $D = D_o*exp(-E_A/kT)$ |
| **Drive in-Doping 2** | | | | Doping for Backside Barriers |
| Temperature (deg C) | $T_c$ | 900 | C | |
| Temperature (K) | T | 1173 | K | deg C + 273 |
| time (min) | $t_m$ | 30 | min | |
| time (sec) | t | 1800 | sec | min*60 |
| Diffusion Coefficient (3rd) | $D_3$ | 1.49E-15 | cm$^2$/sec | $D = D_o*exp(-E_A/kT)$ |
| **Drive in-Oxide 3** | | | | Oxide Growth for Patterning Backside Barriers |
| Temperature (deg C) | $T_c$ | 1000 | C | |
| Temperature (K) | T | 1273 | K | deg C + 273 |
| Time (min) | $t_m$ | 90 | min | |
| Time (sec) | t | 5400 | sec | min*60 |
| Diffusion Coefficient (2nd) | $D_2$ | 2.61E-14 | cm$^2$/sec | $D = D_o*exp(-E_A/kT)$ |
| **Drive in-Doping 3** | | | | Doping for Backside Barriers |
| Temperature (deg C) | $T_c$ | 950 | C | |
| Temperature (K) | T | 1223 | K | deg C + 273 |
| time (min) | $t_m$ | 30 | min | |
| time (sec) | t | 1800 | sec | min*60 |
| Diffusion Coefficient (3rd) | $D_3$ | 6.61E-15 | cm$^2$/sec | $D = D_o*exp(-E_A/kT)$ |

| Front Side P+ Channels (cont.) | Symbols | Value | Units | Notes |
|---|---|---|---|---|
| **Drive in-Oxide 5** | | | | Final Oxide growth for Contacts |
| Temperature (deg C) | $T_c$ | 1000 | C | |
| Temperature (K) | T | 1273 | K | deg C + 273 |
| Time (min) | $t_m$ | 60 | min | |
| Time (sec) | t | 3600 | sec | min*60 |
| Diffusion Coefficient (2nd) | $D_2$ | 2.61E-14 | $cm^2/sec$ | $D = D_o*exp(-E_A/kT)$ |
| **Drive in-Anneal** | | | | Anneal for better metal-substrate contact |
| Temperature (deg C) | $T_c$ | 400 | C | |
| Temperature (K) | T | 673 | K | deg C + 273 |
| Time (min) | $t_m$ | 30 | min | |
| Time (sec) | t | 1800 | sec | min*60 |
| Diffusion Coefficient (3rd) | $D_3$ | 2.50E-27 | $cm^2/sec$ | $D = D_o*exp(-E_A/kT)$ |
| **DT Total** | $Dt_{tot}$ | 3.91E-10 | $cm^2$ | $\Sigma d_i t_i$ |
| **Final Junction Depth** | $x_j$ | 1.691 | um | $x = 2*sqrt(-Dt_{tot}*LN(N_D*sqrt(pi*Dt_{tot})/Q))$ in cm |

| **Back Side N+ Channels** | Symbols | Value | Units | Notes |
|---|---|---|---|---|
| Boltzmann's Constant | k | 8.62E-05 | eV/K | |
| Background Concentration | $N_D$ | 2.15E+11 | Atoms/cm$^3$ | From El-Cat Website-Donor Concentration |
| **Backside N+ Channels (Original Doping)** | | | | Second Diffusion |
| Temperature (deg C) | $T_c$ | 900 | C | |
| Temperature (K) | T | 1173 | K | deg C + 273 |
| Time (min) | $t_m$ | 30 | min | |
| Time(sec) | t | 1800 | sec | min*60 |
| Surface Concentration | $N_o$ | 2.20E+20 | Atoms/cm3 | [9], Figure 4.6 |
| Diffusion Coefficient Constant | $D_o$ | 10.5 | cm$^2$/sec | [9], Table 4.1 |
| Diffusion Coefficient Constant | $E_A$ | 3.69 | eV | [9], Table 4.1 |
| Diffusion Coefficient (Original) | $D_i$ | 1.49E-15 | cm$^2$/sec | $D = D_o*exp(-E_A/kT)$ |
| Dose | Q | 4.06E+14 | cm$^2$/sec | $Q=2*N_o*sqrt(D*t/pi)$ |
| Value of Functions | $N_D/N_o$ | 9.77E-10 | | |
| Inverse erfc | erfc$^{-1}$ | 4.32 | | http://fabweb.ece.uiuc.edu/utilities/erfc/default.aspx |
| Initial Junction Depth | $x_{ji}$ | 0.14 | um | $x_{ji} = 2*sqrt(D_i*t)*erfc^{-1}$ (cm) |
| **Drive in-Oxide 3** | | | | Oxide Growth for Patterning Backside Barriers |
| Temperature (deg C) | $T_c$ | 1000 | C | |
| Temperature (K) | T | 1273 | K | deg C + 273 |
| Time (min) | $t_m$ | 90 | min | |
| Time (sec) | t | 5400 | sec | min*60 |
| Diffusion Coefficient (2nd) | $D_2$ | 2.61E-14 | cm$^2$/sec | $D = D_o*exp(-E_A/kT)$ |
| **Drive in-Doping 3** | | | | Doping for Backside Barriers |
| Temperature (deg C) | $T_c$ | 950 | C | |
| Temperature (K) | T | 1223 | K | deg C + 273 |
| time (min) | $t_m$ | 30 | min | |
| time (sec) | t | 1800 | sec | min*60 |
| Diffusion Coefficient (3rd) | $D_3$ | 6.61E-15 | cm$^2$/sec | $D = D_o*exp(-E_A/kT)$ |
| **Drive in-Oxide 5** | | | | Final Oxide growth for Contacts |
| Temperature (deg C) | $T_c$ | 1000 | C | |
| Temperature (K) | T | 1273 | K | deg C + 273 |
| Time (min) | $t_m$ | 60 | min | |
| Time (sec) | t | 3600 | sec | min*60 |
| Diffusion Coefficient (6th) | $D_6$ | 2.61E-14 | cm$^2$/sec | $D = D_o*exp(-E_A/kT)$ |

| **Back Side N+ Channels (cont.)** | Symbols | Value | Units | Notes |
|---|---|---|---|---|
| **Drive in-Anneal** | | | | Anneal for better metal-substrate contact |
| Temperature (deg C) | $T_c$ | 400 | C | |
| Temperature (K) | T | 673 | K | deg C + 273 |
| Time (min) | $t_m$ | 30 | min | |
| Time (sec) | t | 1800 | sec | min*60 |
| Diffusion Coefficient (7th) | $D_7$ | 2.50E-27 | $cm^2$/sec | $D = D_o*exp(-E_A/kT)$ |
| | | | | |
| **DT Total** | $Dt_{tot}$ | 2.47E-10 | $cm^2$ | $\Sigma d_i t_i$ |
| | | | | |
| **Final Junction Depth** | $x_j$ | 1.335 | um | $x = 2*sqrt(-Dt_{tot}*LN(N_D*sqrt(pi*Dt_{tot})/Q))$ in cm |

| **Back Side P+ Barriers** | Symbols | Value | Units | Notes |
|---|---|---|---|---|
| Boltzmann's Constant | k | 8.62E-05 | eV/K | |
| Background Concentration | $N_D$ | 2.15E+11 | Atoms/cm$^3$ | From El-Cat Website-Donor Concentration |
| **Backside P+ Barriers (Original Doping)** | | | | Second Diffusion |
| Temperature (deg C) | $T_c$ | 950 | C | |
| Temperature (K) | T | 1223 | K | deg C + 273 |
| Time (min) | $t_m$ | 30 | min | |
| Time(sec) | t | 1800 | sec | min*60 |
| Surface Concentration | $N_o$ | 1.20E+20 | Atoms/cm3 | [9], Figure 4.6 |
| Diffusion Coefficient Constant | $D_o$ | 10.5 | cm$^2$/sec | [9], Table 4.1 |
| Diffusion Coefficient Constant | $E_A$ | 3.69 | eV | [9], Table 4.1 |
| Diffusion Coefficient (Original) | $D_i$ | 6.61E-15 | cm$^2$/sec | $D = D_o$*exp($-E_A$/kT) |
| Dose | Q | 4.67E+14 | cm$^2$/sec | Q=2*$N_o$*sqrt(D*t/pi) |
| Value of Functions | $N_D/N_o$ | 1.79E-09 | | |
| Inverse erfc | erfc$^{-1}$ | 4.26 | | http://fabweb.ece.uiuc.edu/utilities/erfc/default.aspx |
| Initial Junction Depth | $x_{ji}$ | 0.294 | um | $x_{ji}$ = 2*sqrt($D_i$*t)*erfc$^{-1}$ (cm) |
| **Drive in-Oxide 5** | | | | Final Oxide growth for Contacts |
| Temperature (deg C) | $T_c$ | 1000 | C | |
| Temperature (K) | T | 1273 | K | deg C + 273 |
| Time (min) | $t_m$ | 60 | min | |
| Time (sec) | t | 3600 | sec | min*60 |
| Diffusion Coefficient (4th) | $D_4$ | 2.61E-14 | cm$^2$/sec | $D = D_o$*exp($-E_A$/kT) |
| **Drive in-Anneal** | | | | Anneal for better metal-substrate contact |
| Temperature (deg C) | $T_c$ | 400 | C | |
| Temperature (K) | T | 673 | K | deg C + 273 |
| Time (min) | $t_m$ | 30 | min | |
| Time (sec) | t | 1800 | sec | min*60 |
| Diffusion Coefficient (5th) | $D_5$ | 2.50E-27 | cm$^2$/sec | $D = D_o$*exp($-E_A$/kT) |
| **DT Total** | $Dt_{tot}$ | 9.41E-11 | cm$^2$ | $\Sigma d_i t_i$ |
| **Final Junction Depth** | $x_j$ | 0.838 | um | x = 2*sqrt($-Dt_{tot}$*LN($N_D$*sqrt(pi*$Dt_{tot}$)/Q)) in cm |

| **Performance Calculations** | Symbols | Value | Units | Notes |
|---|---|---|---|---|
| Boltzmnn's Constant | k | 8.617E-05 | eV/K | |
| Charge of an electron | q | 1.600E-19 | C | |
| Temperature | T | 300.00 | K | |
| Permittivity | $\varepsilon_0$ | 8.850E-14 | F/cm | |
| Silicon Relative Permittivity | $\varepsilon_r$ | 11.90 | | |
| Substrate Thickness | d | 300.00 | µm | |
| Background Concentration | $N_D$ | 2.150E+11 | $cm^{-3}$ | http://www.el-cat.com/silicon-properties.htm |
| Intrinsic Concentration | $n_i$ | 1.000E+10 | $cm^{-3}$ | |
| Acceptor Doping Concentration | $N_A$ | 1.885E+19 | $cm^{-3}$ | $Q_{P+}$/sqrt(pi*$Dt_{tot}$) |
| Donor Doping Concentration | $N_{D+}$ | 1.457E+19 | $cm^{-3}$ | $Q_{N+}$/sqrt(pi*$Dt_{tot}$) |
| Rad4-6 P+ Sheet Resistivity | $R_{S4\text{-}3P+}$ | 36.52 | Ω/square | Measured in Lab |
| Rad4-6 N+ Sheet Resistivity | $R_{S4\text{-}3N+}$ | 20.80 | Ω/square | Measured in Lab |
| Rad4-6 P+ Resistivity | $\rho_{4\text{-}3P+}$ | 6.175E-03 | Ω-cm | $\rho = R_s * x_j$ |
| Rad4-6 N+ Resistivity | $\rho_{4\text{-}3N+}$ | 2.776E-03 | Ω-cm | $\rho = R_s * x_j$ |
| Rad4-6 P+ Concentration | $N_{A4\text{-}3}$ | 1.580E+19 | $cm^{-3}$ | http://www.el-cat.com/silicon-properties.htm |
| Rad4-6 N+ Concentration | $N_{D+4\text{-}3}$ | 2.440E+19 | $cm^{-3}$ | http://www.el-cat.com/silicon-properties.htm |
| Substrate Resistivity | ρ | 2.000E+04 | Ω-cm | |
| Electron Mobility | $\mu_n$ | 1413.87 | $cm^2$/V-s | http://www.el-cat.com/silicon-properties.htm |
| Hole Mobility | $\mu_p$ | 470.46 | $cm^2$/V-s | http://www.el-cat.com/silicon-properties.htm |
| Built in Voltage P+ | $V_{biP+}$ | 0.63 | V | $V_{biP+}$ = kT*ln($N_A N_D/n_i^2$) |
| Built in Voltage N+ | $V_{biN+}$ | 0.62 | V | $V_{biN+}$ = kT*ln($N_{D+} N_D/n_i^2$) |
| Depletion Width P+ (no Bias) | $w_{P+}$ | 62.18 | µm | $w_{P+}$ = sqrt(2*$\varepsilon_o \varepsilon_r$($N_A$+$N_D$)/(q$N_A N_D$)*$V_{biP+}$) |
| Depetion Width N+ (no Bias) | $w_{N+}$ | 61.85 | µm | $w_{N+}$ = sqrt(2*$\varepsilon_o \varepsilon_r$($N_{D+}$+$N_D$)/(q$N_{D+} N_D$)*$V_{biN+}$) |
| Bias to Fully Deplete Substrate | $V_{bias}$ | -14.07 | V | |
| Depletion Width P+ (With Bias) | $w_{P+bias}$ | 300.03 | µm | $w_{P+bias}$ = sqrt(2*$\varepsilon_o \varepsilon_r$($N_A$+$N_D$)/(q$N_A N_D$)*($V_{biP+}$ - $V_{bias}$)) |
| Depletio Width N+ (With Bias) | $w_{N+bias}$ | 61.85 | µm | $w_{N+bias}$ = sqrt(2*$\varepsilon_o \varepsilon_r$($N_{D+}$+$N_D$)/(q$N_{D+} N_D$)*($V_{biN+}$ - $V_{bias}$)) |
| Total Depletion | $w_{tot}$ | 361.88 | µm | $w_{tot}$ = $W_{P+bias}$ + $W_{N+bias}$ |
| Average Electric Field | $E_{AVE}$ | 469.00 | V/cm | |
| Electron Velocity | $v_e$ | 6.631E+05 | cm/s | |
| Hole elocity | $v_h$ | 2.206E+05 | cm/s | |
| Electron Transient Time | $t_e$ | 45.24 | ns | |
| Hole Transient Time | $t_h$ | 135.97 | ns | |

$$V_{bi} = \frac{kT}{q}\ln\frac{N_A N_D}{n_i^2}$$

$$w = \sqrt{\frac{2\varepsilon_r \varepsilon_0 (N_A + N_D)}{q N_A N_D}(V_{bi} - V)}$$

$$\vec{E} = -\nabla V \approx \frac{V}{d}$$

$$\vec{v}(x) = \mu \, \vec{E}(x)$$

$$t = \frac{d}{v} = \frac{thickness}{velocity}$$

**Performance Calculations (cont.)**

| | Symbols | Value | Units | Notes |
|---|---|---|---|---|
| Absorption per EHP | | 3.6 | eV | |
| | | | | |
| Energy vs Range(from Knoll fitted to experimental data) | | | | $R = aE^b$ |
| alpha a | | 1.64 | | |
| alpha b | | 1.64 | | |
| proton a | | 17.85 | | |
| proton b | | 1.62 | | |
| electron a | | 2335 | | |
| electron b | | 1.66 | | |
| | | | | |
| Energy for Range = thickness | | | | |
| Alpha | | 24.0 | MeV | |
| Proton | | 5.7 | MeV | |
| Electron | | 0.291 | MeV | |
| | | | | |
| EHP generated | | | | |
| Alpha | | 6.65E+06 | EHPs | |
| Proton | | 1.59E+06 | EHPs | |
| Electron | | 8.07E+04 | EHPs | |
| | | | | |
| Charge generated | | | | $Q = \# ehp \times q$ |
| Alpha | $Q_\alpha$ | 1.06E-12 | C | |
| Proton | $Q_p$ | 2.54E-13 | C | |
| Electron | $Q_e$ | 1.29E-14 | C | |
| | | | | |
| Current Generated | | | | |
| Electron Alpha | $I_{e\alpha}$ | 2.35E-05 | A | |
| ole Alpha | $I_{h\alpha}$ | 7.83E-06 | A | $I_e = \frac{Q}{t_e}$ |
| Electron Proton | $I_{ep}$ | 5.61E-06 | A | |
| Hole Proton | $I_{hp}$ | 1.87E-06 | A | $I_h = \frac{Q}{t_h}$ |
| Electron Electron | $I_{ee}$ | 2.85E-07 | A | |
| Electron Hole | $I_{eh}$ | 9.50E-08 | A | |
| | | | | |
| EHP/micron | | 80 | EHPs | |
| EHP generated | | 24000 | EHPs | |
| Charge generated | Q | 3.84E-15 | C | |
| Electron curent | Ie | 8.49E-08 | A | |
| Hole current | Ih | 2.82E-08 | A | |

# APPENDIX F

## MATLAB SIMULATION CODE

```
%
%Eric Gowens
%Thesis Calculations-Radiation Sensor
%This program takes in a user inputed bias voltage and calculates the
%device's Electric Field vs. position, Carrier velocities vs. position,
%Carrier transient time vs. position, and and enstimate of the output
%current pulse
%

clear all
Vb = input('Please enter the bias voltage (V): ');
q = 1.6E-19;
k = 8.617E-5;
T = 300;
e0 = 8.85E-14;
er = 11.9;
es = er*e0;
ni = 1E10;
ue = 1413.87;
uh = 470.46;


Y = 0.1:0.1:300;

% Absolute Position of Junctions with origin at top surface (cm)
xjp = 1.691E-4;
xjn = 298.665E-4; % Junction depth = 1.335um

%Dopint Concentrations
NA = 1.885E19;
NB = 2.15E11;
ND = 1.457E19;

%Built In Voltage
VbiP = k*T*log(NA*NB/(ni^2));
VbiN = k*T*log(NB*ND/(ni^2));

% depletion width for P+ doping (cm)
w1 = sqrt(2*es*(NA+NB)/(q*NA*NB)*(VbiP - Vb));
xn1 = w1*(NA/(NA+NB));
xp1 = w1*(NB/(NA+NB));

% depletion width for N+ doping (cm)
w2 = sqrt(2*es*(NB+ND)/(q*NB*ND)*(VbiN - 0));
xn2 = w2*(NB/(NB+ND));
xp2 = w2*(ND/(NB+ND));

for i = 1:3000
    E(i) = 0;
    E1(i) = 0;
    te(i) = 0;
    th(i) = 0;
```

```
end

for i = 1:500
    Pe(i) = 0;
    Ph(i) = 0;
    Pe1(i) = 0;
    Ph1(i) = 0;
end

% Peak electric fields at junction boundries (kV/cm)
Eop = -q*NB*xn1/(es);
% Eon = -q*NB*xp2/(es);

% Electric Field Approximations for P+ Side
i = 1;
for x = 0:(w1*100000)
% E1 = -q*NA*x/(es);  % for (xjp - xp1) to xjp
    E(i) = q*NB*(x/100000)/(es)+Eop;   % for xjp to (xjp + xn1)
    i = i + 1;
end

for i = 1:3000
    E1(i) = E(i);
end

% Electron and Hole Velocities (cm/s)
for i = 1:3000
    Ve(i) = -ue*E(i);
    Vh(i) = -uh*E(i);
end

for i = 1:3000
    for j = 1:i
        te(i) = te(i) + 1E-5/Ve(j);
        th(i) = th(i) + 1E-5/Vh(j);
    end
end

figure(1);
subplot(2,2,1); plot(Y,E1);
axis([0 300 E(1) 0]);
title('Electric Field vs. Position');
xlabel('Position (um)');
ylabel('Field Strength (V/cm)');

subplot(2,2,2); plot(Y,Ve);
axis([0 300 0 Ve(1)])
title('Velocity vs. Position');
xlabel('Position (um)');
ylabel('Velocity (cm/s)');
hold;
plot(Y,Vh, 'color', 'red');
hold;
```

```
thmax = th(3000);

subplot(2,2,3); plot(Y,te);
axis([0 300 0 1.5E-7]);
title('Transient Time vs. Position');
xlabel('Position (um)');
ylabel('Time (s)');
hold;
plot(Y,th, 'color', 'red');
hold;

%Code to predict output pulse from carrier transient times
for i = 1:500
    for j = 1:3000
        if te(j) < 1E-9
            if te(j) > 0
                Pe(i) = Pe(i) + 1;
            end
        end
    end

    for j = 1:3000
        te(j) = te(j) - 1E-9;
    end

    for j = 1:3000
        if th(j) < 1E-9
            if th(j) > 0
                Ph(i) = Ph(i) + 1;
            end
        end
    end

    for j = 1:3000
        th(j) = th(j) - 1E-9;
    end
end

for i = 1:500
    Pe1(i) = (8*Pe(i)*q)/1E-9;
    Ph1(i) = (8*Ph(i)*q)/1E-9;
end


subplot(2,2,4);
plot(Pe1); hold;
title('Output Current Pulses');
xlabel('Time (ns)');
ylabel('Current (A)');
axis([0 150 0 .25E-6]);
plot(Ph1,'color','red'); hold;
```

# APPENDIX G

## GENERATION 4 SENSOR DATA

**Table G.1** Generation 4 sensor output at -10V, -20V, and -30V bias with the laser aimed at the approximate center of the sensor

| Channel | -10 V Bias (V) | -20 V Bias (V) | -30 V Bias (V) |
|---|---|---|---|
| **F-1** | -0.338 | -0.322 | -0.150 |
| **F-2** | -0.334 | -0.322 | -0.152 |
| **F-3** | -0.334 | -0.322 | -0.154 |
| **F-4** | -0.338 | -0.322 | -0.158 |
| **F-5** | -0.340 | -0.326 | -0.166 |
| **F-6** | -0.342 | -0.330 | -0.172 |
| **F-7** | -0.350 | -0.340 | -0.180 |
| **F-8** | -0.362 | -0.354 | -0.192 |
| **F-9** | -0.372 | -0.372 | -0.210 |
| **F-10** | -0.376 | -0.368 | -0.206 |
| **F-11** | -0.360 | -0.352 | -0.190 |
| **F-12** | -0.350 | -0.340 | -0.176 |
| **F-13** | -0.344 | -0.330 | -0.168 |
| **F-14** | -0.340 | -0.328 | -0.166 |
| **F-15** | -0.340 | -0.324 | -0.156 |
| **F-16** | -0.340 | -0.322 | -0.150 |
| **B-1** | 0.050 | 0.050 | 0.020 |
| **B-2** | 0.200 | 0.350 | 0.200 |
| **B-3** | 0.075 | 0.075 | 0.050 |
| **B-4** | 0.010 | 0.010 | 0.010 |
| **B-5** | 0.075 | 0.075 | 0.175 |
| **B-6** | 0.075 | 0.075 | 0.150 |
| **B-7** | 0.010 | 0.010 | 0.010 |
| **B-8** | 0.350 | 0.350 | 0.150 |
| **B-9** | 5.340 | 5.440 | 5.440 |
| **B-10** | 0.050 | 0.075 | 0.100 |
| **B-11** | 0.010 | 0.010 | 0.010 |
| **B-12** | 0.010 | 0.010 | 0.010 |
| **B-13** | 0.075 | 0.075 | 0.050 |
| **B-14** | 0.075 | 0.075 | 0.050 |
| **B-15** | 0.075 | 0.100 | 0.050 |
| **B-16** | 0.075 | 0.050 | 0.050 |

**Table G.2** Generation 4 sensor output at -10V, -20V, and -30V bias with the laser aimed at the bottom left corner of the sensor

| Channel | -10 V Bias (V) | -20 V Bias (V) | -30 V Bias (V) |
|---|---|---|---|
| **F-1** | -0.308 | -0.300 | -0.140 |
| **F-2** | -0.304 | -0.296 | -0.138 |
| **F-3** | -0.304 | -0.296 | -0.136 |
| **F-4** | -0.300 | -0.296 | -0.134 |
| **F-5** | -0.300 | -0.296 | -0.136 |
| **F-6** | -0.300 | -0.296 | -0.138 |
| **F-7** | -0.300 | -0.286 | -0.140 |
| **F-8** | -0.300 | -0.286 | -0.144 |
| **F-9** | -0.300 | -0.286 | -0.146 |
| **F-10** | -0.304 | -0.300 | -0.154 |
| **F-11** | -0.308 | -0.304 | -0.160 |
| **F-12** | -0.314 | -0.306 | -0.166 |
| **F-13** | -0.320 | -0.310 | -0.168 |
| **F-14** | -0.324 | -0.314 | -0.170 |
| **F-15** | -0.332 | -0.326 | -0.176 |
| **F-16** | -0.328 | -0.318 | -0.156 |
| **B-1** | 0.050 | 0.075 | 0.075 |
| **B-2** | 0.132 | 0.300 | 0.200 |
| **B-3** | 4.960 | 5.00 | 5.040 |
| **B-4** | 0.010 | 0.010 | 0.010 |
| **B-5** | 0.120 | 0.050 | 0.124 |
| **B-6** | 0.150 | 0.050 | 0.124 |
| **B-7** | 0.010 | 0.010 | 0.010 |
| **B-8** | 0.310 | 0.300 | 0.134 |
| **B-9** | 0.010 | 0.010 | 0.010 |
| **B-10** | 0.150 | 0.075 | 0.050 |
| **B-11** | 0.010 | 0.010 | 0.010 |
| **B-12** | 0.010 | 0.010 | 0.010 |
| **B-13** | 0.150 | 0.075 | 0.025 |
| **B-14** | 0.150 | 0.075 | 0.050 |
| **B-15** | 0.100 | 0.090 | 0.042 |
| **B-16** | 0.120 | 0.050 | 0.020 |

**Table G.1** Generation 4 sensor output at -10V, -20V, and -30V bias with the laser aimed at the bottom right corner of the sensor

| Channel | -10 V Bias (V) | -20 V Bias (V) | -30 V Bias (V) |
|---|---|---|---|
| **F-1** | -0.304 | -0.296 | -0.138 |
| **F-2** | -0.300 | -0.292 | -0.138 |
| **F-3** | -0.300 | -0.290 | -0.140 |
| **F-4** | -0.300 | -0.286 | -0.140 |
| **F-5** | -0.296 | -0.290 | -0.140 |
| **F-6** | -0.300 | -0.286 | -0.142 |
| **F-7** | -0.300 | -0.290 | -0.146 |
| **F-8** | -0.300 | -0.290 | -0.150 |
| **F-9** | -0.300 | -0.292 | -0.150 |
| **F-10** | -0.304 | -0.294 | -0.154 |
| **F-11** | -0.304 | -0.298 | -0.160 |
| **F-12** | -0.308 | -0.300 | -0.160 |
| **F-13** | -0.312 | -0.304 | -0.162 |
| **F-14** | -0.320 | -0.312 | -0.168 |
| **F-15** | -0.328 | -0.322 | -0.174 |
| **F-16** | -0.320 | -0.312 | -0.150 |
| **B-1** | 0.050 | 0.050 | 0.050 |
| **B-2** | 0.200 | 0.300 | 0.180 |
| **B-3** | 0.050 | 0.075 | 0.050 |
| **B-4** | 0.010 | 0.010 | 0.010 |
| **B-5** | 0.075 | 0.075 | 0.150 |
| **B-6** | 0.075 | 0.075 | 0.150 |
| **B-7** | 0.010 | 0.010 | 0.010 |
| **B-8** | 0.310 | 0.300 | 0.180 |
| **B-9** | 0.075 | 0.075 | 0.050 |
| **B-10** | 0.075 | 0.075 | 0.050 |
| **B-11** | 0.010 | 0.010 | 0.010 |
| **B-12** | 0.010 | 0.010 | 0.010 |
| **B-13** | 0.050 | 0.050 | 0.050 |
| **B-14** | 0.050 | 0.050 | 0.075 |
| **B-15** | 0.050 | 0.100 | 0.150 |
| **B-16** | 4.86 | 4.96 | 4.72 |

**Table G.3** Generation 4 sensor output at -10V, -20V, and -30V bias with the laser aimed at the top left corner of the sensor

| Channel | -10 V Bias (V) | -20 V Bias (V) | -30 V Bias (V) |
|---|---|---|---|
| **F-1** | -0.212 | -0.278 | -0.144 |
| **F-2** | -0.226 | -0.280 | -0.148 |
| **F-3** | -0.226 | -0.256 | -0.138 |
| **F-4** | -0.214 | -0.244 | -0.128 |
| **F-5** | -0.206 | -0.240 | -0.122 |
| **F-6** | -0.200 | -0.236 | -0.114 |
| **F-7** | -0.196 | -0.232 | -0.112 |
| **F-8** | -0.194 | -0.232 | -0.108 |
| **F-9** | -0.190 | -0.228 | -0.106 |
| **F-10** | -0.190 | -0.228 | -0.104 |
| **F-11** | -0.190 | -0.224 | -01.04 |
| **F-12** | -0.190 | -0.228 | -0.104 |
| **F-13** | -0.190 | -0.228 | -0.104 |
| **F-14** | -0.190 | -0228 | -0.106 |
| **F-15** | -0.190 | -0.236 | -0.106 |
| **F-16** | -0.190 | -0.236 | -0.108 |
| **B-1** | 0.100 | 0.100 | 0.100 |
| **B-2** | 0.120 | 0.300 | 0.300 |
| **B-3** | 3.080 | 3.740 | 3.640 |
| **B-4** | 0.010 | 0.010 | 0.010 |
| **B-5** | 0.050 | 0.075 | 0.100 |
| **B-6** | 0.050 | 0.050 | 0.100 |
| **B-7** | 0.010 | 0.010 | 0.010 |
| **B-8** | 0.182 | 0.238 | 0.100 |
| **B-9** | 0.020 | 0.050 | 0.020 |
| **B-10** | 0.020 | 0.050 | 0.020 |
| **B-11** | 0.010 | 0.010 | 0.010 |
| **B-12** | 0.010 | 0.010 | 0.010 |
| **B-13** | 0.020 | 0.050 | 0.020 |
| **B-14** | 0.020 | 0.050 | 0.020 |
| **B-15** | 0.020 | 0.075 | 0.050 |
| **B-16** | 0.020 | 0.020 | 0.020 |

**Table G.4** Generation 4 sensor output at -10V, -20V, and -30V bias with the laser aimed at the top right corner of the sensor

| Channel | -10 V Bias (V) | -20 V Bias (V) | -30 V Bias (V) |
|---|---|---|---|
| **F-1** | -0.368 | -0.364 | -0.186 |
| **F-2** | -0.380 | -0.380 | -0.214 |
| **F-3** | -0.400 | -0.404 | -0.244 |
| **F-4** | -0.400 | -0.404 | -0.248 |
| **F-5** | -0.380 | -0.380 | -0.230 |
| **F-6** | -0.368 | -0.364 | -0.214 |
| **F-7** | -0.360 | -0.354 | -0.202 |
| **F-8** | -0.356 | -0.346 | -0.196 |
| **F-9** | -0.352 | -0.350 | -0.190 |
| **F-10** | -0.352 | -0.346 | -0.184 |
| **F-11** | -0.352 | -0.346 | -0.180 |
| **F-12** | -0.352 | -0.346 | -0.176 |
| **F-13** | -0.352 | -0.346 | -0.164 |
| **F-14** | -0.352 | -0.346 | -0.166 |
| **F-15** | -0.352 | -0.348 | -0.164 |
| **F-16** | -0.356 | -0.348 | -0.160 |
| **B-1** | 0.050 | 0.075 | 0.020 |
| **B-2** | 0.200 | 0.400 | 0.200 |
| **B-3** | 0.100 | 0.075 | 0.050 |
| **B-4** | 0.010 | 0.010 | 0.010 |
| **B-5** | 0.100 | 0.100 | 0.150 |
| **B-6** | 0.100 | 0.100 | 0.144 |
| **B-7** | 0.010 | 0.010 | 0.010 |
| **B-8** | 0.350 | 0.390 | 0.150 |
| **B-9** | 0.100 | 0.100 | 0.050 |
| **B-10** | 0.100 | 0.100 | 0.050 |
| **B-11** | 0.010 | 0.010 | 0.010 |
| **B-12** | 0.010 | 0.010 | 0.010 |
| **B-13** | 0.075 | 0.075 | 0.075 |
| **B-14** | 0.100 | 0.120 | 0.150 |
| **B-15** | 0.075 | 0.120 | 0.120 |
| **B-16** | 5.760 | 5.800 | 5.840 |